In situ Development of Cs3Sb Photocathodes for Optical Near-Field Electron Microscopy

Beest, Jay te

In situ Development of Cs_3Sb Photocathodes for Optical Near-Field Electron Microscopy

THESIS

submitted in partial fulfillment of the
requirements for the degree of

MASTER OF SCIENCE
in
PHYSICS

Author :	J.T. te Beest
Student ID :	s2003201
Supervisor :	Prof.dr.ir. S.J. van der Molen
Second corrector :	Prof.dr. J.M. van Ruitenbeek

Leiden, The Netherlands, October 30, 2024

In situ Development of Cs_3Sb Photocathodes for Optical Near-Field Electron Microscopy

J.T. te Beest

Huygens-Kamerlingh Onnes Laboratory, Leiden University
P.O. Box 9500, 2300 RA Leiden, The Netherlands

October 30, 2024

Abstract

In this thesis, we investigate the co-deposition of cesium and antimony to develop efficient Cs_3Sb photocathodes for Optical Near-field Electron Microscopy (ONEM), aiming to achieve ultra-smooth, ultra-thin photocathodes with high quantum efficiency. The project involved implementing, designing and calibrating new equipment, such as a Dual Cluster Source evaporator, a Quartz Crystal Monitor, a QE measurement setup and a custom transfer arm extension with sample heater for temperature controlled growth. All the equipment is installed in the preparation chamber of the ESCHER LEEM, where we have successfully grown several photocathodes. Ultimately, a photocathode grown in the preparation chamber, with a measured moderate QE of around 0.3% at 450 nm light, has been successfully utilized for the first time to obtain an ONEM image of a biological sample.

Contents

Version of October 30, 2024– Created October 30, 2024 - 11:40

List of abbreviations

AFM Atomic Force Microscopy

ARPES Angle-Resolved Photoemission Spectroscopy

ARRES Angle-Resolved Reflection Electron Spectroscopy

DCS Dual Cluster Source

DOS density of states

EDX energy-dispersive X-ray spectroscopy

ESCHER Electronic Structural and Chemical Nanoimaging in Real Time

FWHM full width at half maximum

LEED Low Energy Electron Diffraction

LEEM Low Energy Electron Microscopy

MMT mirror mode transition

ONEM Optical Near-Field Electron Microscopy

QCM Quartz Crystal Monitor

QE quantum efficiency

ROI region of interest

SEM Scanning Electron Microscopy

TC thermocouple

UHV ultra high vacuum

WF work function

Chapter 1

Introduction

Microscopy and imaging techniques have played a crucial role in advancing our understanding of materials at the nanoscale. By providing a detailed visualization of structures and surfaces, these techniques have enabled researchers to study a wide range of phenomena, from biological processes to the behavior of (new) nanomaterials. Traditional imaging methods, such as the optical microscope or the electron microscope, are powerful tools that offer high resolution and deep insights into material properties on the scale of a few hundred nanometers and several nanometers respectively. However, exposure to high-energy electron beams can lead to sample degradation or show effects such as charging, altering the very features that are of interest to us.

One emerging technique that addresses these concerns is Optical Near-Field Electron Microscopy (ONEM) [1], [2]. ONEM is an innovative approach that combines the high resolution capabilities of electron microscopy with the non-invasive nature of optical imaging. Unlike conventional electron microscopy, ONEM utilizes the optical near-field response of a sample to excite electron from a nearby low work function photocathode layer through the photoelectric effect. This allows for high resolution (~ 5 nm) imaging without the need for high-energy electron beams that can damage the sample, as the optical light has an relatively low photon energy. This method is especially beneficial for imaging delicate or highly reactive materials, as it minimizes the interaction between the imaging tool and the sample, thereby preserving the sample's original structure, properties and dynamics. Conveniently, ONEM can be carried out in an already existing Low Energy Electron Microscopy (LEEM) instrument. In this instrument, the excited low energy photoelectrons from the photocathode can be imaged in the same way as the low energy electrons from the electron gun. One of the main differences here is the need for a photocathode.

A photocathode is a specialized thin film, typically composed of metal alloy or semiconductor material, designed to emit electrons when illuminated by light. For effective ONEM operation, photocathodes must exhibit certain desirable properties. Key among these are high quantum efficiency (QE), which is the ability to convert incident photons into emitted electrons; ultra-smooth surface morphology, which minimizes electron scattering; and a applicable stoichiometry and thickness. These characteristics are essential because even a small increase in surface roughness can drastically affect the electron emission process [3]–[5], rendering the photocathode unsuitable for ONEM, while it might still function well in applications like solar cells where surface smoothness is less critical. The ability to control the growth conditions to achieve these optimal surface qualities is vital for advancing the performance of photocathodes in high-resolution imaging systems.

This research focuses on a particularly promising two-metal alloy for a useful photocathode which is Cs_3Sb. This compound/alloy has a low work function (1.6 eV [6]) with a high quantum efficiency, meaning that relative many photoelectrons can be excited with relatively little energy [7]–[10]. It would be a considerable result if not only photoelectrons are excited after illumination with blue light (high energy photons), but also for green and red light (low energy photons). To achieve this, it is essential to systematically produce photocathodes that are clean, high-quality, and properly stoichiometric. Namely, a key challenge in working with photocathodes is their sensitivity to environmental conditions, particularly exposure to oxygen [3] and moisture. Many photocathodes are made from materials that will quickly degrade when exposed to air, making them highly fragile and difficult to study using conventional imaging techniques. To circumvent this problem the photocathodes are grown *in situ*, i.e. in the same ultra high vacuum (UHV) environment where they will be studied or used for ONEM.

The objective of this research is to enhance the preparation chamber of the Electronic Structural and Chemical Nanoimaging in Real Time (ESCHER) LEEM in Leiden by implementing instruments for the co-deposition of cesium (Cs) and antimony (Sb) via thermal evaporation onto a temperature-controlled sample. This setup should allow for precise monitoring of the evaporation rates and measurement of the QE of the resulting photocathodes. Additionally, the synthesized photocathodes will be analyzed within the LEEM to assess their effectiveness for ONEM imaging by analyzing their work function and surface smoothness.

This thesis starts with an overview of the background of applied principles and techniques in this research, after which the practical procedures will be discussed regarding these different subjects. This consists of reviewing the design, calibration and utilization of the aforementioned components. The following chapter will show several more general samples and discuss the results, among which an ONEM sample. Finally, the research will be concluded in the final chapter, which also offers an outlook with suggestions for future research.

Version of October 30, 2024– Created October 30, 2024 - 11:40

Chapter 2

Background

This chapter will provide the theoretical background of the principles utilized in this research, which consists of LEEM and ONEM and the growing and characterization methods of photocathodes.

2.1 ONEM/LEEM

2.1.1 LEEM

Optical microscopes lack the resolution for imaging of nanometer scale details and other imaging techniques are too slow (e.g. Atomic Force Microscopy (AFM)) or too damaging (e.g. Scanning Electron Microscopy (SEM)) for delicate samples. LEEM is an advanced technique that aims to avoid these troubles by employing electrons in the energy range of just 0-100 eV, whilst ensuring high spatial resolution. The interaction between these electrons and the sample surface provides detailed information about its topography, composition, and real-time imaging of dynamic processes, such as (epitaxial) growth, phase transitions, or chemical reactions. LEEM is especially useful for studying the surfaces of materials, as the low-energy electrons are sensitive to surface structures, allowing for imaging with a ~ 5 nm resolution [1].

The low energy electrons that are used for LEEM are produced by a cold field emission gun with an energy of 15 keV. These electrons are focused by several electromagnetic lenses and subsequently deflected over 90° towards a sample of interest (left side of Fig. 2.1), which is kept at -15 kV plus some sample bias voltage, such that the landing energy of the electrons is within this low energy range on the order of eV [11], [12]. If the landing energy is negative, the electrons never reach the sample and reverse their course, which is called the mirror mode. When the sample bias is then increased from negative to positive values during measurements there will be a small energy range in which the electrons will finally start hitting the sample, which is called the mirror mode transition (MMT). The reflected electrons are then re-accelerated to 15 keV and deflected again towards an aberration-correcting electron mirror. Lastly, the electrons are deflected again and proceed towards the channel plate that amplifies the electron signal. The signal is subsequently passed through a phosphor screen and ends in CCD camera, from which a real space image is constructed. The contrast aperture can be operated to choose for bright and dark field imaging. To sustain the high electric field between the last electron lens and the biased sample (10 kV/mm), the pressure inside needs to be very low, in the UHV range ($\leqslant 1.0 \cdot 10^{-8}$ mbar).

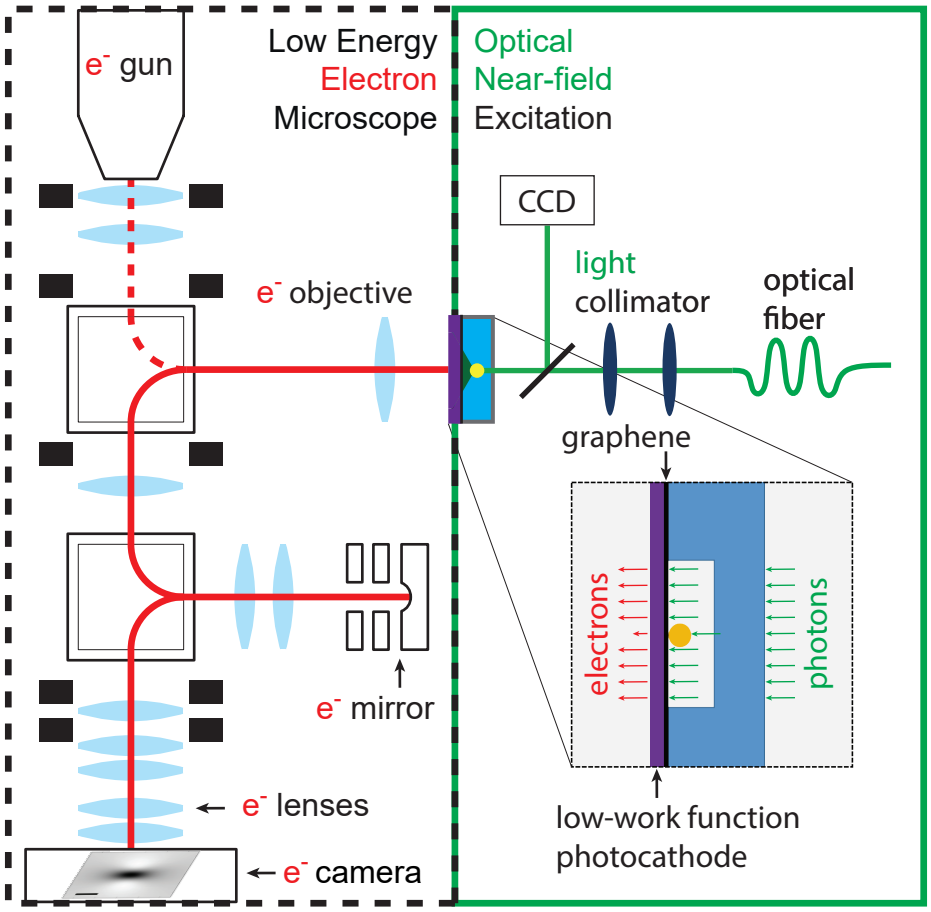

Figure 2.1: *LEEM and ONEM in one setup. An example of a liquid cell sample close to a photocathode, that provides the photoelectrons for LEEM imaging. Figure from [2].*

2.1.2 LEED

Low Energy Electron Diffraction (LEED) on the other hand is used to determine the atomic structure of crystalline layers. In LEED, a beam of low-energy electrons (typically 20-200 eV) is directed at the surface of interest, after which the electrons are diffracted by the surface atoms. The resulting diffraction pattern provides information in reciprocal space about the periodic arrangement of atoms on the surface layers, i.e. the crystalline structure and characteristics such as the lattice spacing.

2.1.3 ONEM

Optical Near-field Electron Microscopy (ONEM) operates by illuminating a sample of interest with optical light that is located on the backside of a nearby photocathode. Hereby an optical near-field is generated around the surface of the sample and this localized field excites electrons within the photocathode, leading to electron emission from its surface. These emitted electrons are then collected into the LEEM setup as described in section *LEEM* and used to form an image of the sample. This process not only delivers super-resolution images via the near-field, but also preserves the integrity of sensitive materials by employing low-energy visible light photons and thus avoiding the high-energy interactions that often cause sample degradation in conventional electron microscopy. For example, the energy of green light photons (E_{photon} = 2.3 eV at λ = 532 nm) lies well below the absorption band of most proteins [2]. A simple schematic of how ONEM is incorporated in the LEEM instrument is shown in Figure 2.1.

2.2 Photocathodes and their characterization

The photocathode that is used for the photon-to-photoelectron conversion is of great importance in ONEM. Its surface should be sufficiently smooth such that no image artifacts are introduced during the conversion. This can happen due to the bending of the electric field lines close to the photocathode due to physical roughness of the surface [13], [14]. Furthermore, the photocathode must also convert photons to photoelectrons with high efficiency. Here, one needs to find the balance between signal strength and thickness, as a thicker photocathode can increase the efficiency and thus the signal strength. However, due to the increased thickness the photocathode lies further away from the sample and its near-field, thus the resolution decreases. Finally, the elemental composition, i.e. the atoms and their configuration that make up the photocathode influence its properties.

The goal in this research is to grow such a photocathode through thermal co-evaporation of Cs and Sb in a Cs_3Sb ratio/stoichiometry, which is selected because of its interesting properties as an alloy such as its high efficiency [6], [8], [15], [16]. Our choice for co-evaporation is encouraged by a paper from Feng *et al.* from 2017 [4]. Here, they show a much smoother alkali antimonide photocathode when grown through co-evaporation (near atomic smoothness) compared to sequential growth.

2.2.1 Work function

To excite an electron from a photocathode into the vacuum, an incident photon needs to have a certain minimum amount of energy to achieve this. This minimal energy is called the work function of a material, which is defined as:

$$\Phi = E_{vac} - E_F \tag{2.1}$$

Here, Φ is the work function, E_{vac} the vacuum energy and E_F the Fermi energy of the material. The Fermi energy is defined as the energy level below which all electron states are filled at absolute zero temperature. It's a reference point in the energy distribution of electrons in a solid. The vacuum energy is the potential energy an electron would have if it were completely free from the influence of the solid. In practical terms, it is the energy level of an electron that has just escaped the material into the vacuum, yet it still senses the potential from the surface. Namely, at infinity this potential would go to zero.

Furthermore, an electron is able to escape from the material, if it were to be excited by a photon with sufficient energy. This energy needs to be enough such that the electron can overcome any inelastic scattering events (other electrons) within the surface layers, on top of the work function. Two important characteristics for this process are the *inelastic mean free path* l_{inel} and the *penetration depth* d_p [17]. Both concepts represent a length scale over which the attenuation of the amount is a factor $\frac{1}{e}$, the former for photoelectrons and the latter for incident photons. l_{inel} and d_p vary with the material and the frequency of the light that is used. For visible light the value of l_{inel} lies between the two to five nm, whereas d_p is on the order of tens of nm. From this it can be concluded that an increasingly thick photocathode at some point will not yield more photoelectrons, as they cannot escape the surface. Besides the requirement of sufficient energy, a photoelectron must also contain sufficient momentum perpendicular to the surface, or it will be absorbed back into the material.

Remarkably, it is possible to lower the work function of a surface, by for example deposition of Cs onto the surface. Φ is lowered because Cs is highly electropositive, meaning it easily

donates electrons to the surface. In this way, there is a positively charged surface and an accumulation of electrons just beneath it, forming a dipole layer. The produced electric field at the surface effectively lowers the energy barrier for an electron to escape into the vacuum, thus lowering the work function.

This electropositivity is a characteristic of alkali-metals and therefore alkali semiconductors typically have for low work functions which can function as visible-light photocathodes. For example, Cs combined with Sb can form a highly efficient photocathode, with a stoichiometry of approximately Cs_3Sb. Cs has a work function of $\Phi_{Cs} = 2.1$ eV, Sb of $\Phi_{Sb} = 4.5$ eV and Cs_3Sb of $\Phi_{Cs_3Sb} = 1.6$ eV [6]. The low work function of the alkali-antimonide alloys is due to the combined effects of the electropositive nature of an alkali metal and the electronic structure of the compound, which facilitates efficient electron emission.

2.2.2 LEEM work function analysis

LEEM data consists of an voltage bias sweep (EGYM) from typically -10 eV to 30 eV bias. The MMT is expected to lie around the 0 eV in these sweeps due to pre-calibration. Before the MMT, the reflectivity is circa 1, as no electrons make it to the surface and are reflected back beforehand. Then during the bias increase, the reflectivity will drop as more and more electrons will reach the surface. Therefore, the IV curve will drop down in value, from which the MMT can be determined. If the electrons were truly monochromatic, the intensity drop would be infinitely steep, as a step function. In reality the electron energy is distributed according to the Fowler-Nordheim distribution, which can be approximated by a Gaussian with an energy spread $\sigma \approx 0.25$ eV [13].

The MMT is determined through fitting an error function the the IV curve of the voltage sweep. The error function used for the fit is given in Equation (2.2) [13]:

$$I(V_0) = \frac{I_{\mathrm{MM}} - I_{\mathrm{LEEM}}}{2} \cdot \mathrm{erfc}\left(\frac{V_0 - V_{\mathrm{MMT}}}{\sqrt{2}\sigma}\right) + I_{\mathrm{LEEM}} \tag{2.2}$$

Where I_{MM} represents the intensity in mirror mode, before the drops commences and all electrons are reflected back, and I_{LEEM} the intensity after the MMT transition in LEEM mode. When the data is properly normalized, these values are often roughly 1 and 0 respectively. These parameters can simply be taken from the data. Now, V_{MMT} can be extracted from the fit. This value represents the value of the middle of the MMT itself, where the work function (WF) of the sample is defined.

To investigate the homogeneity of a photocathode, we create a spatially resolved WF heatmap. As a pre-processing measure of the data, the images of the voltage sweep are put through a channelplate correction and a drift correction. In order to keep the computational time reasonable, the LEEM images are scaled down by averaging over slices of typically 4x4 pixels. For each such a square, the average IV curve is determined and the error function fit (Eq. (2.2)) is carried out. All these separate work functions are stored in a 2D array, which can be visualized via a heatmap.

An example of a WF heatmap is provided in Figure 2.2C. Sample 125 is important as a WF reference sample for which a LEEM IV sweep was taken. It consisted of solely a Si-110 substrate without a photocathode on it. It should be noted that the later photocathodes were grown on Si-100 substrates, but the influence of this difference should be marginal. The region of interest (ROI) was divided into 8x8 pixel squares and for each of these the WF was computed through the error function fit to its IV curve (Eq. (2.2)) as illustrated in

Figure 2.2B. The heatmap indicates an average WF of -0.84 eV, whereas literature states that silicon oxide has a WF of circa 5.0 eV [18]. This means that there is approximately a 5.84 eV offset between the EGYM value of the LEEM that is displayed in the data here and the actual WF. We opt to set the substrate WF at 0 eV such that its MMT is centered around 0 eV. This means that the later WF data is translated +0.84 eV to align with the substrate reference WF.

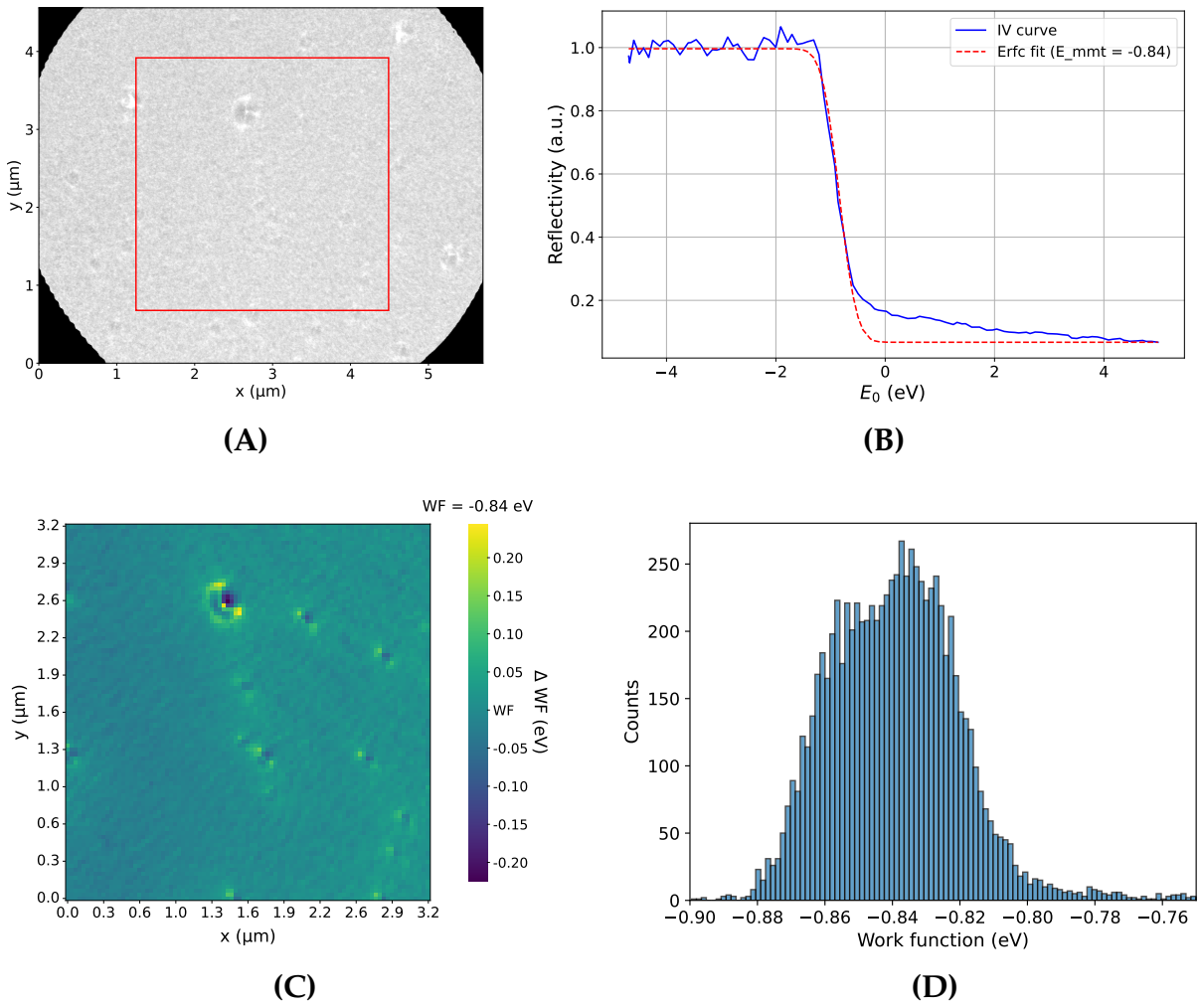

Figure 2.2: *LEEM data of sample 125, the substrate reference sample.* **(A)** *ROI of the substrate.* **(B)** *Erfc fit to the average IV curve of all squares within the ROI.* **(C)** *Heatmap of normalized WFs in the ROI.* **(D)** *Histogram of the work functions inside the ROI.*

The distribution of the WFs for all squares is shown in the histogram in Figure 2.2D. The overall shape of the distribution is quite well defined, with a small plateau around the -0.85 eV and a full width at half maximum (FWHM) of circa 70 meV. This could be explained by the defects/impurities that were present on the substrate, as they are responsible for both lower WF values in their center and higher WF values surrounding them compared to the average WF. This was also a useful experiment to determine the cleanliness of such substrates, which should perhaps be annealed or flashed beforehand. Overall, the surface WF is quite uniform, except for localized regions of impurity, which too only differ circa 0.2 eV from the bulk WF.

2.2.3 LEED analysis

We have primarily taken LEED IVs of photocathodes grown during the later runs, which might be less useful than LEEM IVs as it does not provide us information about the uniformity or homogeneity of the photocathode, but rather about its crystallinity. Unfortunately, we do not observe any higher order diffraction spots in these samples. This indicates that the photocathodes have no crystalline structure as of now and we weren't growing them epitaxially. The IV curve is obtained by monitoring the intensity of this central diffraction spot during the sweep, resulting in a single IV curve. In the same fashion as for the LEEM IVs, an error function (see Eq. (2.2)) is fitted to the curve which yields a single work function for the whole photocathode. While this approach doesn't give a full picture of the layer properties, it can still be useful when analyzed alongside QE data to identify potential correlations.

Without using a contrast aperture, the IV curves can exhibit unusual behavior as secondary electrons are being generated, causing the curve to bend upwards beyond the initial reflectivity. That is because new electrons are generated, as is visible in the intensity and size of the Ewald sphere. Investigating this phenomenon in the future could be insightful. Carried out properly, an Angle-Resolved Photoemission Spectroscopy (ARPES) experiment can yield valuable information about the band structure of the grown photocathode.

2.2.4 Electronic band structure

A key reason for the use of these alkali semiconductors is the corresponding electronic band structure of their energy levels and the associated density of states (DOS), see Figure 2.3.

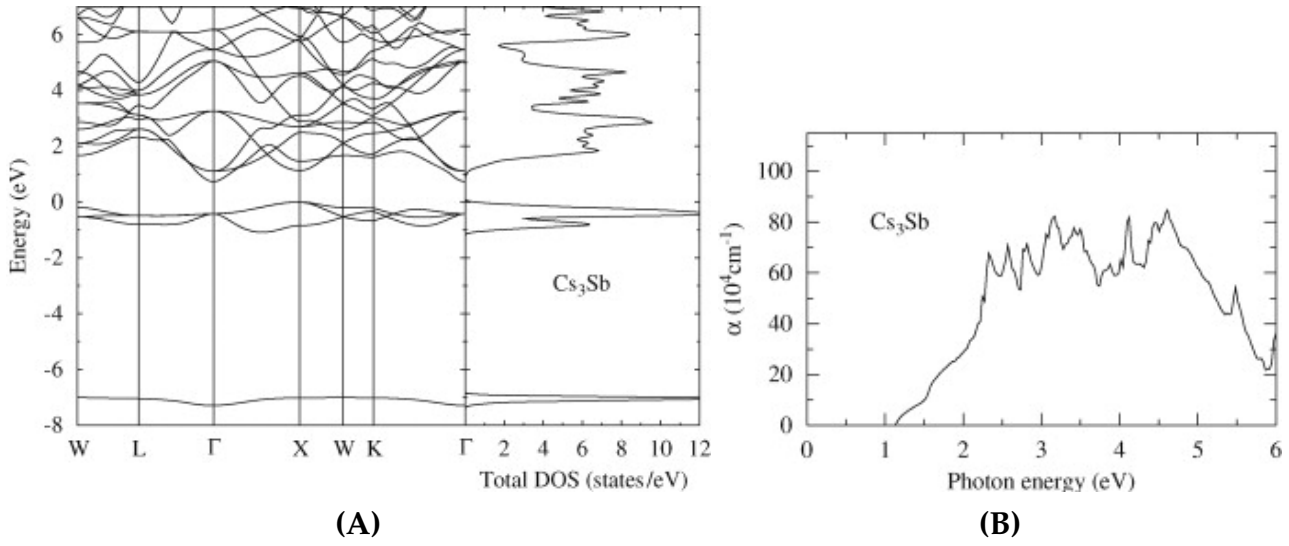

Figure 2.3: **(A)** *DOS and band structure of Cs_3Sb.* **(B)** *Absorption coefficient of Cs_3Sb. Both images are taken from [6].*

The right side of Figure 2.3A shows why Cs_3Sb as semiconductor operates so well as a photocathode. There is a large sea of electrons available for excitation just below the Fermi energy, which is defined here at 0 eV. These electrons can make the jump to some vacant bands with less than 2 eV in energy. This is also shown more clearly in Figure 2.3B. Again, this energy gap resides well within the visible light energy range as even red photons ($\lambda =$ 660 nm) have an energy of 1.88 eV. Clearly, Cs_3Sb would be a proper choice for an ONEM photocathode as they show high absorption over the whole optical light energy range (1.7 – 3.2 eV)

2.2.5 Quantum Efficiency

The aforementioned efficiency for photocathodes is called the quantum efficiency, regarding the conversion efficiency of photocathodes via the photoelectric effect. Strictly speaking, it can be defined in two manners: the internal QE and the external QE. However, we will stick to the experimentally simpler external QE throughout this thesis and call this the QE for simplicity. In short, the internal QE is defined as the ratio between the produced photoelectrons and the total of photons absorbed by the photocathode itself. This, therefore, takes external losses into account, which is very dependent on the optical setup. For the external QE we take the total number of emitted photons. This number of photons per second is obtained by measuring the power of the laser P(W) and dividing it by the photon energy E_{photon} (J). Meanwhile, the number of electrons is obtained by measuring the total photocurrent per second I(A) and dividing this by the elementary charge e. In formula form:

$$QE = \frac{\#\text{electron/s}}{\#\text{photon/s}} = \frac{I/e}{P/E_{\text{photon}}} = \frac{I \cdot h \cdot c}{P \cdot e \cdot \lambda} \tag{2.3}$$

Here, h denotes the Planck constant and c the speed of light. Conveniently, Equation (2.3) can be simplified by rewriting the second fraction, as the photon energy E_{photon} in Joule divided by the elementary charge e in Coulomb yields the photon energy in eV. The more simple QE formula is then:

$$QE = \frac{I[\text{A}] \cdot E_{\text{photon}}[\text{eV}]/[\text{C}]}{P[\text{W}]} \tag{2.4}$$

As an indication of the QE as a function of stoichiometry, the spectral response of Cs_3Sb and CsSb is shown in Figure 2.4. Our goal is to grow a photocathode with approximately a 3:1 stoichiometry for optimal QE. However, even if we fall short in achieving the ideal evaporation ratio between Cs and Sb, we can still expect to observe some photocurrent from the photocathode using 450 nm laser light. Parzyck *et al.* [3] report a QE just below 1% at 450 nm for a thin CsSb photocathode, which would likely already be sufficient for ONEM. They further report that the computed work functions from their models of CsSb and Cs_3Sb are 2.19 eV and 1.65 eV respectively.

Furthermore, the ratio of QE for different wavelengths can also provide an estimate of the stoichiometry for good quality photocathodes, as reported by Pavlenko *et al* [8]. They monitor the ratio of QE_{405nm}/QE_{532nm} for different Cs:Sb flux ratios through a PID controlled evaporation scheme. By maintaining the QE ratio at roughly 2, they ensured to be within a small offset of the optimal 3:1 stoichiometry. This could also be a convenient measure for this research to quickly determine the photocathode's stoichiometry.

2.2.6 Thermal evaporation

The Cs_3Sb photocathode is grown with a Dual Cluster Source (DCS) evaporator, which contains two separate crucibles that are also thermally shielded from each other via active water cooling. The crucibles are heated by applying a large current to the coils around the crucibles, thus starting the evaporation of its constituents. The Cs is captured in a cesium molybdate salt, as pure Cs is highly reactive and reacts violently with the moisture of the air and thus cannot be easily handled outside vacuum otherwise.

Version of October 30, 2024– Created October 30, 2024 - 11:40

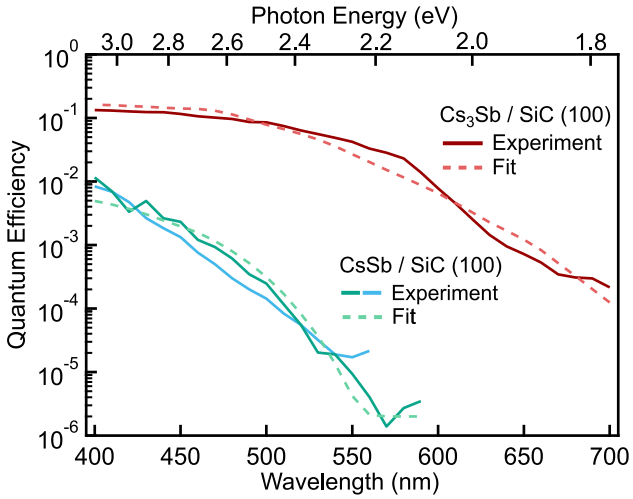

Figure 2.4: *Comparison of QE for Cs_3Sb and CsSb over a range of visible light wavelengths. The results are shown for three different photocathodes: 8 nm (blue), 18 nm (green) and 45 nm (red). Taken from [3].*

A typical evaporation pressure is on the order of $10^{-6} - 10^{-7}$ mbar. For pure Cs this pressure is already achieved at room temperature. However, since the Cs is trapped inside a salt, the temperature needed is a lot higher, roughly 580 °C. For pure Sb, as it is used in this research, the pressure is achieved at roughly 330 °C [19].

The deposition is influenced by many factors, such as the evaporation rate, the type of crucible which contains the material, the distance to the target and thereby the spread of the evaporated beam of metal. As the latter two are a constant in the setup, the most important variable is the evaporation rate, which is altered through the temperature.

2.2.7 QCM

This rate is measured via a Quartz Crystal Monitor (QCM), which works by measuring the change in frequency of a vibrating quartz crystal to determine mass changes at its surface. The quartz crystal is coated with a thin gold film, and when a small amount of material is deposited onto this film, it changes the oscillation frequency of the crystal. The QCM operates based on the piezoelectric effect, where an alternating electrical field causes the crystal to vibrate, with its resonant oscillation frequency located in the MHz regime. The resonance frequency shift is proportional to the mass added or removed from the crystal surface, enabling highly sensitive mass measurements on the order of nanograms. Since the properties of the crystal and the deposited material are known, it is possible to determine the thickness of the layer that is grown on the QCM. The QCM should be placed sufficiently close to the sample, then it is possible to determine the tooling factor of the system, which is the constant factor between the measured thickness via the QCM and the actual thickness of the layer on the target. The latter can be determined with a profilometer or an AFM.

The change in frequency Δf is linearly proportional to the change in mass Δm, as when more mass is deposited onto the crystal its resonance frequency decreases. The formula describing this relation is called the Sauerbrey equation [20]:

$$\Delta f = -\frac{2f_0^2}{A\sqrt{\rho_q \mu_q}}\Delta m \tag{2.5}$$

Here, f_0 is the fundamental resonance frequency of the crystal in Hz, typically on the order of 5 MHz, A [cm^2] is the active crystal area that can be deposited onto, ρ_q is the density of quartz [g/cm^3] and μ_q is the shear modulus [g/cm s^2] or rigidity of quartz. As all the parameters in the fraction are constants, the formula is often simplified to $\Delta m = -C\Delta f$, with the C the mass sensitivity constant [ng/cm^2 Hz]. C denotes how much ng of material needs to be deposited per cm^2 to shift the frequency with one Hz. For a 5 MHz quartz crystal this is approximately 17.7 ng/cm^2 Hz. The Sauerbrey equation holds under the following three conditions: the deposited mass must be evenly distributed across the surface, this mass should also be rigid of nature and the overall frequency change cannot exceed 5% of the initial resonance frequency.

2.2.8 EDX

It is imperative to know if the photocathode that is grown actually consists of the elements you expect in the expected ratios. For this, we use energy-dispersive X-ray spectroscopy (EDX). This analytical technique can determine the elemental composition of a material by bombardment with high energy electrons. These are also available in the LEEM setup, where a collimated electron beam is generated in the very beginning and accelerated to 15 keV. When these high-energy electrons hit the photocathode, they can excite inner-shell electrons from the atoms that compose the photocathode. This electron vacancy is then filled by an electron from a higher-energy shell and the energy difference between the two shells is emitted in a high energy photon, an X-ray. These X-rays have unique energy levels that correspond to specific elements, allowing the EDX detector to identify which elements are present in the photocathode.

The photocathode is typically bombarded for several minutes, during which the data can be accumulated and an energy distribution of the photons can be plotted. Peaks are expected to show up on the corresponding elemental energies, which should be taken from literature. A SEM with an EDX detector can even create a spatial map of the photocathode, showing the elemental quantities per area that compose the photocathode. Importantly, the data thus shows only the intensity or the amount of X-rays that are detected. To get to the actual thickness or amount of atoms that compose the layer, one needs to study the ratios of the elemental peaks or compare the counts to a reference material present on the sample.

The EDX system attached to the main chamber of the LEEM has only recently become operational and is still undergoing testing in certain aspects. Our primary goal is to use it for qualitative stoichiometric analysis. Performing quantitative measurements is more challenging because it requires an aforementioned reference standard material with known composition and thickness. This is necessary to accurately determine the amount of Cs and Sb from a peak fit to the EDX spectrum and comparing the peak heights and their ratios. We've employed 10 keV electrons, which have sufficient energy to obtain the Cs and Sb X-rays as these lie around the 4 keV.

We use EDX to estimate the stoichiometry by comparing the heights of the α peaks in the spectrum, as the peak height is proportional to the element's abundance. As for the Cs_3Sb photocathode, we aim for a Cs:Sb ratio close to 3:1. However, several factors need to be accounted for and a ZAF correction needs to be carried out. This corrects for the atomic number (Z) which influences backscattering and the penetration factor of the electrons, absorption (A) within the photocathode of the produced X-rays and lastly fluorescence (F) whereby false positive X-rays are produced in the layer. Besides, the efficiency of the detector differs per wavelength and yet needs to be determined before proper measurements

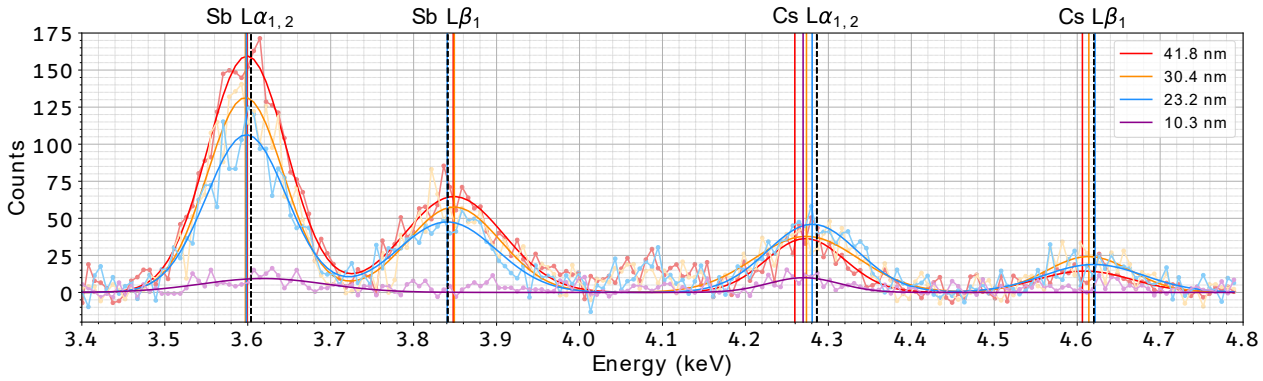

Figure 2.5: *A visual comparison of the intensity peaks obtained from a 10 min EDX measured of Cs_3Sb photocathodes of different thicknesses.*

will take place, which has not been performed for our EDX.

At this stage, there are too many unknowns to draw definitive conclusions from our data. For the thin photocathodes that we have, we must compensate for multiple scattering events within the photocathode. This makes many assumptions for simplicity incorrect. What we can confirm is the presence of Cs and Sb in the samples, along with potential contaminants. We can also roughly estimate the abundance of these elements by looking at the relative heights of the peaks. Longer measurement times, around 10 minutes, seem necessary for more reliable data, as shorter acquisitions (e.g. 2 minutes) do not provide sufficient counts.

Figure 2.5 provides a comparison of four evaporation runs in which we have grown photocathodes of different thicknesses. For Sb, we see that a thicker photocathode yields a higher peak, both for L$\alpha_{1,2}$ and Lβ_1. For Cs, however, the peak height does not comply with the expected order as from the thickness. Regardless, it is not yet possible to give a stoichiometry indication, as we have not compensated for the several factors as mentioned above, which can clearly influence the results.

Chapter 3

Practical procedures

To achieve the *in situ* growth of a Cs_3Sb photocathode within the LEEM UHV environment, we researched, designed and installed several new components, particularly in the preparation chamber of the ESCHER LEEM at the Kamerlingh Onnes Laboratory, Leiden University. Accordingly, each section of this chapter will cover both the engineering aspects and the calibration measurements of each component.

To reiterate: to grow and analyze Cs_3Sb photocathodes inside the preparation chamber of the LEEM, we need a source of evaporation, a QCM to monitor the evaporation rate, a setup to measure QE during and after growth and a transfer arm that contains a temperature-controlled sample stage.

3.1 Preparation chamber

The preparation chamber (hereafter: prep chamber) is located above the transfer chamber and is a cylinder with a diameter of circa 25 cm and a height of circa 20 cm. The prep chamber has three sizes of flanges: the small 40CF, the medium 63CF and the large 100CF, where the numbers denote the diameter of the flange in mm. Importantly, several flanges of the prep chamber are already taken. The geometry of the alterations that we will make during the research is also important, as for example it is optimal for the new transfer arm with a heatable stage to be placed opposite of the evaporator such that the evaporated beam arrives as perpendicular as possible to the sample surface. The laser part of the QE setup is then preferably placed close to the evaporator, such that the laser can conveniently shine onto the sample. The QCM typically has two orientations in which it can be bought, with the crystal perpendicular or parallel to the tubes it is attached to. This means that to measure the evaporation rate optimally, the flange for the QCM needs to be located either opposite of the evaporator or on a 90° angle, such that the crystal is perpendicular to the beam of evaporated ions.

Keeping all of these requirements in mind, we have decided on the following configuration for the additions to the prep chamber of the LEEM, as shown in Figure 3.1. In Figure 3.1C and 3.1D, the flange for the evaporator is shown in lilac, the flange for the QCM in olive, the flange for the QE setup in black, the flange for the transfer arm in red and finally the flange for the electrical feedthrough on top of the chamber in yellow.

We have determined what the configuration of all components onto the prep chamber will be and a schematic of this final arrangement is illustrated in Figure 3.2. Note that at the

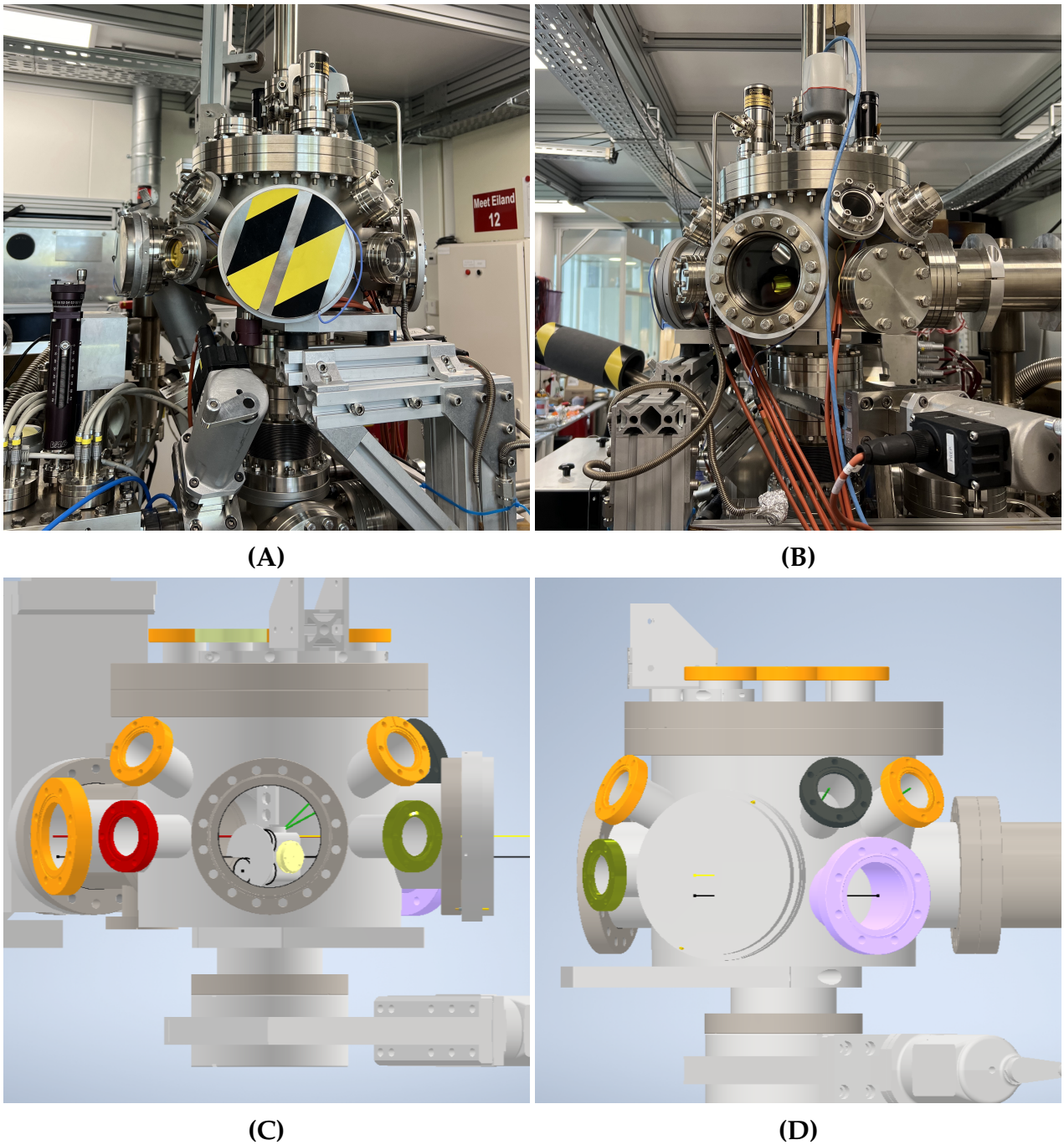

Figure 3.1: *The preparation chamber of the ESCHER LEEM in Leiden, as seen from different angles. The colored flanges correspond to: lilac = DCS evaporator, olive = QCM, black = QE, red = transfer arm, yellow (on top) = electrical feedthrough.* **(A)** *&* **(C)** *and* **(B)** *&* **(D)** *show different sides of the prep chamber, both in real life and as Inventor schematic respectively for clarity.*

time of writing there are no 3D designs available of the QCM and the QE system, which are mounted onto the prep chamber at the olive and black colored flanges respectively.

Figure 3.3A provides a visual overview of the component layout inside the prep chamber during an evaporation run. At the center of the image, a sample is shown loaded onto the transfer arm. This photo was taken before the final version of the transfer arm extension was installed, thus at this point we were using a simpler stainless steel version without a heater or thermocouple (TC). The small black wire attached to the transfer arm is the ground connection for the QE. To the left of the sample, the QCM crystal is visible inside its casing,

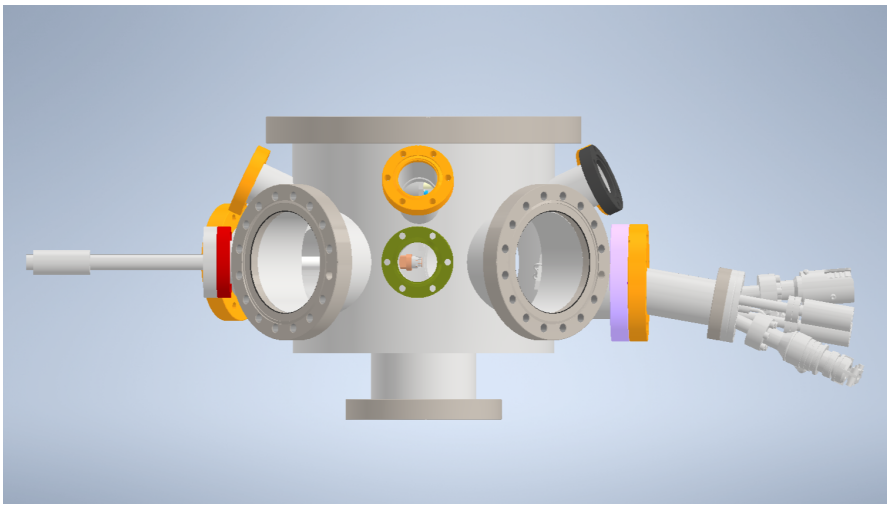

Figure 3.2: *An overview of the prep chamber as given in Figure3.1, but now with the transfer arm (red flange) and the DCS (lilac flange) added to the schematic. The QCM (olive flange) and the QE system (black flange) have no 3D Inventor design yet.*

positioned far enough to the left to not hinder the vertical transfer arm during transfers.

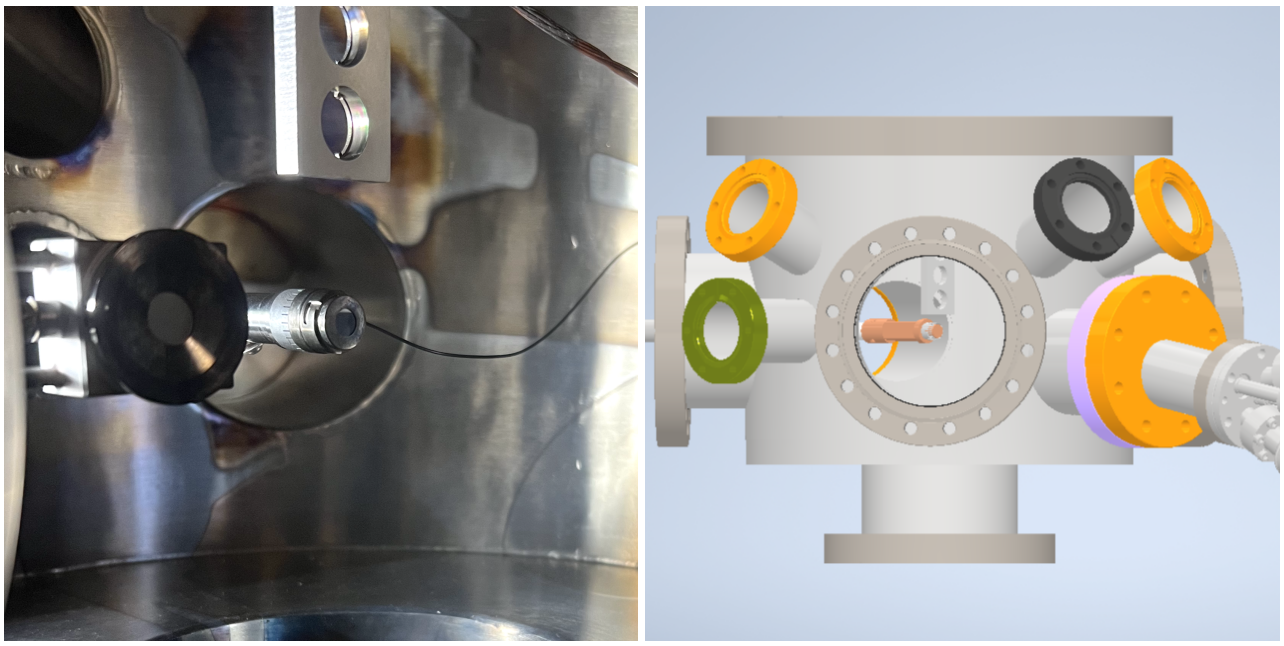

(A) **(B)**

Figure 3.3: *Visualization of the interior of the prep chamber as seen through the viewport adjacent to the DCS.* **(A)** *shows a real-life image, while* **(B)** *presents a schematic from the same perspective of the prep chamber.*

The sample holder of the vertical transfer arm is partially visible above the sample. Lastly, as the DCS is aimed directly at the sample on the transfer arm (see also Fig. 3.6B), there is deposition build-up visible on the chamber walls in the background behind the transfer arm.

3.2 Dual Cluster Source evaporator

3.2.1 Practical

The co-deposition or co-evaporation of the Cs and Sb will be carried out with the Dual Cluster Source evaporator (DCS 40-2x1-14-2S-SF-2105114 from MBE-komponenten*, see Figure 3.4). It is mounted onto the lilac flange in Figure 3.1D. This evaporator contains two separate slots for a small crucible, in which the evaporation material can be loaded. The crucibles have a nominal volume of circa 0.6 mL and can be of several materials, depending on the material that you want to evaporate from it. In our case, we have opted for a quartz (SiO_2) crucible for the Cs and Al_2O_3 for Sb. The crucibles are thermally shielded through active water cooling and the DCS has two individual rotary shutters. This means that it is possible to heat up Cs and Sb simultaneously, yet evaporate them separately, which is useful for tuning the evaporation rate or growing solely a Cs or Sb layer. The DCS contains two type C TCs. These TCs consist of two different metals and because of the temperature difference of the hot and the cold metal components, a voltage gradient develops between the two. This voltage is a measure for the temperature of the crucible, which needs to be calibrated beforehand.

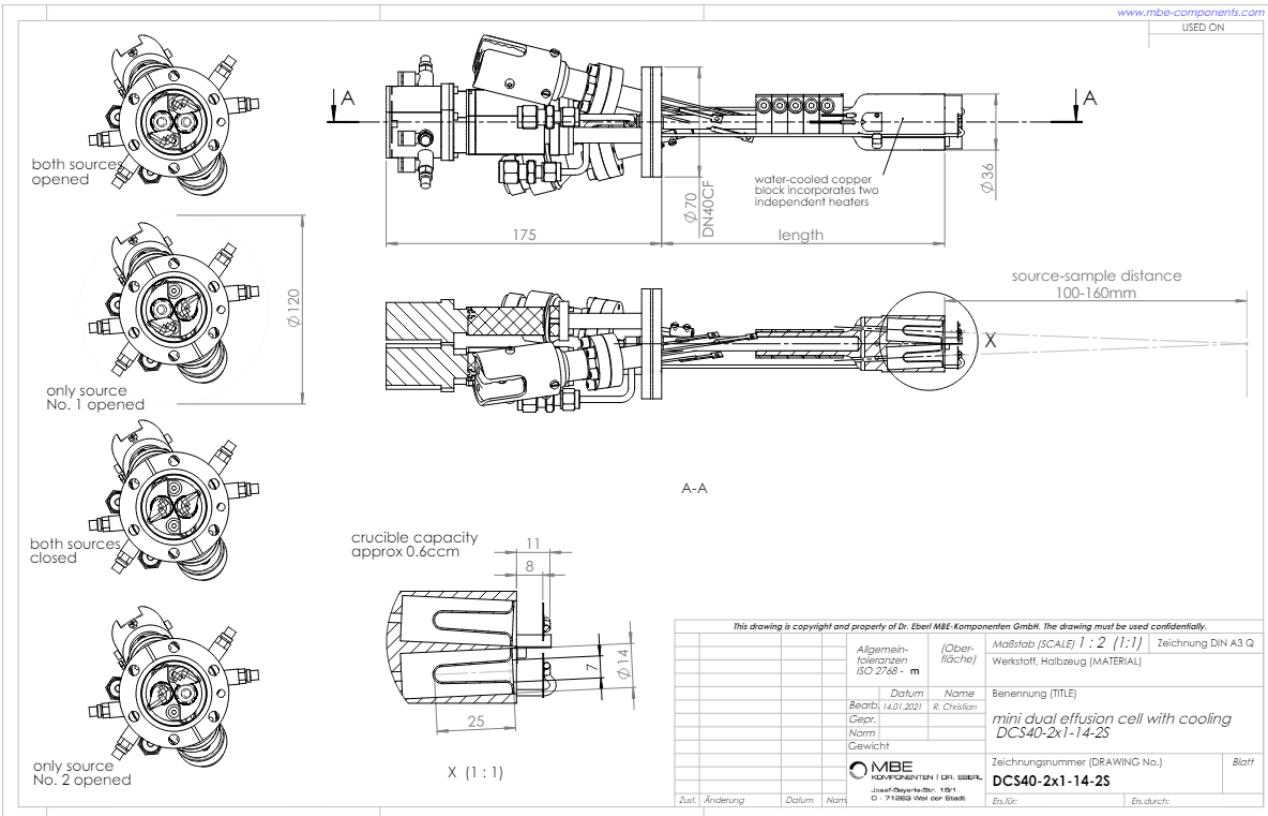

Figure 3.4: *Schematic of the DCS evaporator used in this research, shown from different angles.*

In collaboration with the Fine Mechanical Department (FMD), we have designed a custom flange extension that positions the DCS at a slight upward angle, aimed precisely at the center of the preparation chamber. This upward orientation is needed for preventing material leakage from the crucibles and for directing the evaporant beam directly at the sample.

Additionally, the DCS is actively cooled with water at all times such that both crucibles are thermally separated and that there is less radiation from the heated DCS into the chamber.

*https://www.mbe-komponenten.de/source-clusters/dcs/

Finally, there are two TC pins, as there are two crucibles which need to be monitored separately. Both TCs are type C (Tungsten-Rhenium alloy), which is convenient for monitoring very high temperatures up to 2315 °C. We have utilized an already present MBE power supply with a PID temperature controller (Eurotherm 3500 series) which was pre-calibrated for a type C TC. We have not carried out any reference temperature measurements with for example an optical pyrometer, yet we do take the temperature values of the TC as a useful measure.

Towards the end of the research we have tried reading out the crucible temperature with another apparatus, an OMNI-controller (SIMEX SRD-99) that can also be connected to a computer for logging of the data. As there was not sufficient time for finalizing this coding part, the temperature was logged manually during evaporation sessions and written up as a reference. The power supply (Delta Elektronika DC) data was also manually noted when the current was changed.

3.2.2 Calibration

After the final position and orientation of the DCS was determined, it could be connected to the cooling water, thermocouple read-out and the power supplies. The DCS can only be calibrated in conjunction with the QCM, which is treated in more detail in the following section.

The QCM provides us the rate linked to the temperature and thus current we put through the DCS. During the first evaporation run, we set the current for the Cs to 5A, yielding an uncalibrated rate of roughly 1 Å/s and a crucible temperature of 700°C according to the TC. This proved to be much too high, as during a subsequent run no Cs evaporation was measured, meaning the crucible was already depleted of Cs. Other work typically uses very low evaporation rates, such as Pavlenko *et al* who use a 0.03 Å/s rate [8]. We consequently determined to aim for sub 0.1 Å/s growth rates for Cs evaporation, which proved difficult as the graphs given by the QCM software were quite noisy, even after replacing the BNC cable and adding water cooling to the QCM.

After several evaporation runs we started the co-evaporation by utilizing a second power supply for the Sb. Sb seemed to be more stable in its rate, whereas Cs still depletes more quickly. As we opted for a 3:1 stoichiometry, we aimed for a 3:1 evaporation rate of Cs:Sb. Naturally, the thickness of a film of Cs or Sb doesn't provide us the stoichiometry of the Cs_3Sb photocathode directly, as a Sb film might differ in density from a Cs film. The stoichiometry can in fact be invoked from QE measurements [8] and EDX.

This total rate should be low enough such that the Cs does not deplete too quickly and that the grown layer is sufficiently smooth. This total co-deposition rate typically was of the order 0.3 - 0.4 Å/s, constituting for a large proportion of Cs. This was achieved by supplying roughly 3.0 - 3.2 A to the Sb crucible ($\approx$ 450°C) and 4.2 - 4.4 A to the Cs crucible ($\approx$ 650°C). These are the final ranges for the runs, a result of almost 40 evaporation runs. At these temperatures, the materials did not deplete too quickly as the Cs would last typically one week, consisting of several runs. Furthermore, the temperature of the crucibles seemed stable, although it did increase circa 10°C every time the shutters were closed for a few minutes when a sample transfer needed to be carried out or we needed only one of the Cs or Sb for rate calibration.

At these typical values, there was still a background evaporation rate measurable when the shutters were closed, of roughly 0.02 Å/s. This is because the shutters of the DCS are

Version of October 30, 2024– Created October 30, 2024 - 11:40

mounted quite far from the crucible and some evaporant escapes to the side of this shutter. However, since the QCM is at an angle to the left and the sample itself is directly located in line of the crucible, the evaporant supposedly cannot reach the sample directly in this situation because of the shutter, whereas some of it can in fact reach the QCM.

Rather than using the rate/time graph of the software, we looked at the thickness/time graph as the slope of this graphs indicates the rate. This was particularly useful to verify whether a change in current resulted in the desired change in evaporation rate. This method was not very precise, yet as we were in the beginning stages of the research it was sufficient.

Some typical evaporation runs are shown in Figure 3.5. The evaporation rates are notably different in value and in stability. The orange and blue runs are the most stable in rate (Fig. 3.5A), which is also reflected in the constant slopes of the thickness in Figure 3.5B. The rates were tuned by altering the current if deemed necessary.

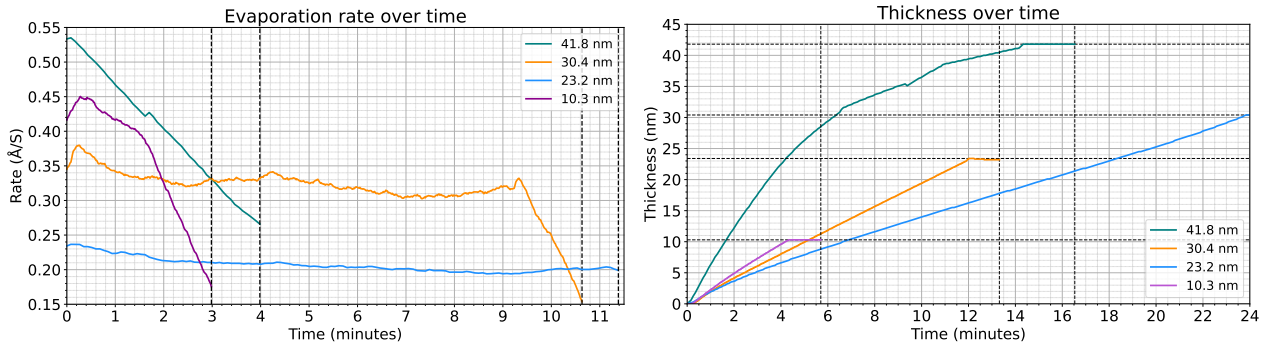

(A) **(B)**

Figure 3.5: *Rate and thickness data of four evaporation runs, all with a different end thickness.* **(A)** *Smoothened evaporation rates.* **(B)** *Film thickness over time.*

Besides the deposition rate of the QCM, the pressure inside the chamber is also a proper indication of the evaporation rate. We use a PKR251 Pfeiffer pressure gauge, positioned on top of the prep chamber. The pressure is a more direct rate of the evaporation rate, as the QCM only measures the deposition rate onto the QCM and does not compensate for a different sticking coefficient of the substrate with respect to the quartz. Furthermore, on the QCM we actually grow multiple layers of Cs and Sb sequentially over multiple evaporation runs, whereas the silicon oxide substrate is clean in every run. However, the evaporant beam also is not directed onto the pressure gauge directly. Thus similar as to the QCM, a calibration should be carried out to determine the factor between the measured rate and the actual rate.

3.3 Quartz Crystal Monitor

3.3.1 Practical

During evaporation, it is imperative to know the rate of evaporation, or rather deposition, such that you can verify how thick the grown photocathode is and what the ratio is between the Cs and Sb evaporation rates. To monitor these rates, we employ a Quartz Crystal Monitor or Quartz crystal Microbalance (QCM), specifically an Inficon Front Load Single Sensor, as shown in Figure 3.6.

This sensor further consists of a casing that has water tubes connected to it for active cooling, this reduces any thermal noise that occurs due to the hot evaporated ions onto the crystal

and casing. The tubes and the cable are fixed to a CF40 flange (see Fig. 3.6A), which is then mounted onto the prep chamber of the LEEM on the olive colored flange in Figure 3.1C. The corresponding gold-coated quartz crystals have a printed contact pattern on it and when placed delicately and correctly into the retainer with a crystal snatcher, it makes a closed circuit. Finally the crystal holder is placed on top of the crystal, leaving a central circular part exposed onto which evaporant can be deposited.

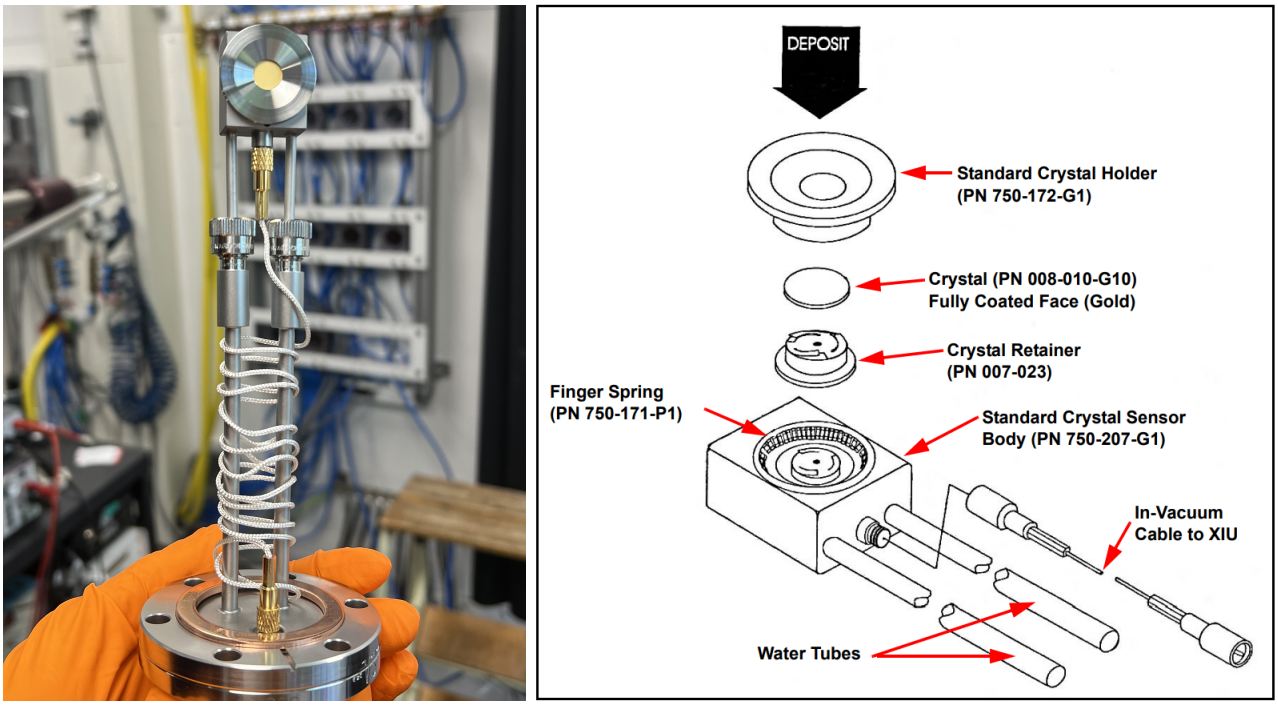

(A) **(B)**

Figure 3.6: *The Quartz Crystal Monitor.* **(A)** *The QCM. On top, the crystal in its holder. It is connected via a cable to the flange, where on the other side it is connected to the QCM controller and computer. Everything visible on this side of the flange is the in-vacuum side.* **(B)** *Schematic of the innerworkings of the in-vacuum QCM part.*

The QCM line of sight makes a 90° angle with that of the DCS (lilac flange Fig. 3.1D) and resides in the same horizontal plane as that of the sample. As the sample is in the middle of the beam that comes from the DCS, the QCM is somewhat to the left side of it as seen from the DCS. The center of the QCM crystal is located approximately three cm away from the sample. As from the perspective of the DCS, the QCM is located circa 9° to the left. It is important that the exposed crystal surface is orientated perpendicular to the evaporant stream from the DCS, as otherwise the crystal life will be negatively affected and unwanted oscillatory modes can develop. These issues occur because of the uneven material distribution across the crystal surface as to the side that is angled away from the source receives less material. Altogether this will lead to inaccurate or incorrect output values.

As mentioned before, the evaporation rate may differ from the deposition rate, as not all evaporated ions necessarily adhere to the surface they encounter. The QCM measures the deposition rate, but we do not have a precise understanding of the ratio between evaporated and deposited ions. Additionally, since the QCM's position is fixed, a standard *tooling factor* can be determined to relate the thickness measured by the QCM to the actual thickness on the sample. These thicknesses differ, because the QCM is positioned to the side of the beam, while the sample is located at the center and thus should receive more evaporant. The tooling factor can be determined by measuring the photocathode thickness using a

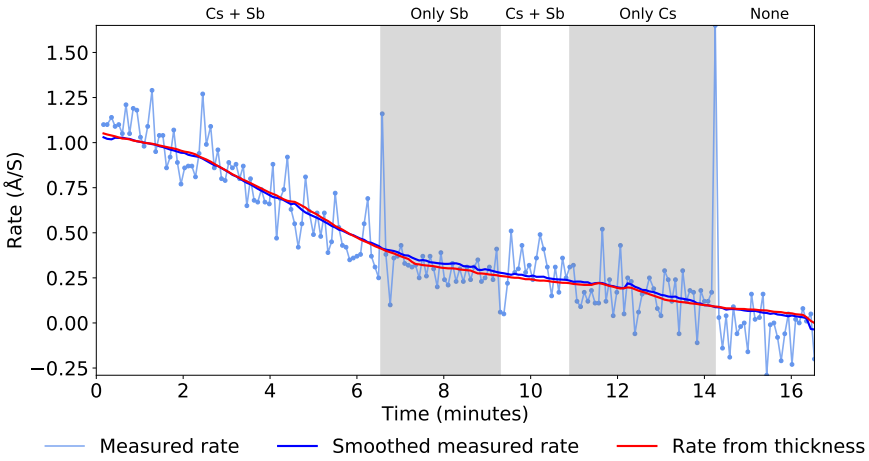

Figure 3.7: *A comparison of the noisy rate and the smoothened rate of evaporation run 36.*

profilometer or AFM and comparing it to the QCM reading. This step was not completed during the present research, but should be a straightforward task for future work.

3.3.2 Calibration

A large portion of the calibration is already discussed in the calibration section of the DCS (*Calibration*), as the calibration of the DCS evaporator required the presence of the QCM. Consequently, these systems were calibrated and optimized simultaneously. As mentioned, the QCM software provided quite a noisy evaporation rate, which made it hard to accurately read out the evaporation rate by eye during runs. This noise did not decrease after connecting the QCM to the water tubes for cooling. This was also expected, as the noise should not be thermally induced as the temperature of the QCM would not be very high. The noise could stem from electronic connections or simply mechanical noise in the LEEM setup. The QCM manual states that the noise level is of order 0.03 Å/s, which is slightly less than the noise we observe in the system (0.05 Å/s). This noise is, however, too high to verify by eye whether the evaporation rate is 0.08 Å/s, which we often required for the Sb rate. Figure 3.7 provides an example of the noisiness of the evaporation rate as given by the QCM controller output. The red line represents the rate as computed from the derivative from the thickness graph, which evidently is a better indicator of the rate than the rate graph itself. The smoothened rated is computed through averaging over several datapoints.

As for the maintenance, we have replaced the crystal only once during one month of usage. At the time the crystal life was around 80%, yet we noticed some dirt, supposedly evaporant, on the crystal holder and on the crystal itself, so we replaced it preventively.

Also, the QCM software requires a density or material input through which the deposited layer thickness can be computed. This differs per material, as the measured frequency indicates a deposited mass, which is then converted to a volume (i.e. thickness) via the density. Cs has a density of 1.886 g/cm^3, Sb of 6.684 g/cm^3 and Cs_3Sb of circa 4.26 g/cm^3.

Further work should make use of a script that directly reads out the frequency as provided by the QCM controller (STM-2 Thin Film Rate/Thickness Monitor). These values can then be converted to a mass change and thus a growth rate through the Sauerbrey equation (Eq. (2.5)). The data was saved with a 1 second interval and consisted of the rate, the thickness and the frequency. The final rate was computed with a rolling average function, as the calculated rate by the software was too noisy and thus unclear.

3.4 Quantum Efficiency setup

3.4.1 Practical

The QE is an important measure of a photocathode, as it tells you if you could use such a photocathode for actual ONEM applications. Conveniently for this research, there was already a QE setup available in the LEEM which was designed during a previous project. With this in place, several initial proof-of-concept measurements were carried out. This setup needed some fine tuning to fit in our current setup and required a rework of the code that is used to instruct the power supply and the laser that handles the data logging properly. One of the major parts is the custom in-vacuum part designed with the FMD which contains the U-shaped anode. This anode can be rotated towards or away from the sample and has its electrical connections to outside the vacuum through one of the small flanges on top of the prep chamber. A Keithley 2450 source measure unit is used for reading and logging of the photoelectron current from the photocathode and for supplying the 40V potential between the sample and the anode. This voltage is required to help the excited electrons from the photocathode reach the anode.

The laser that we use for the QE measurements is the FISBA READYBeam Ind1 which is capable of emitting 450 nm (blue), 520 nm (green) and 660 nm (red) light, with a typical center wavelength tolerance of $\pm$ 10 nm. The photons are emitted into a fiber that is screwed onto a beam collimator. The photons subsequently leave the collimator and are either transmitted, reflected or absorbed by the viewport window that they encounter, before reaching the vacuum and finally the sample. The collimator is mounted onto an optical table, which also has a large ring fixed on it that is placed over a CF40 flange. The collimator can be adjusted such that the laser beam hits the target by rotating the optical table around the flange, tuning the height of the collimator pin or rotating the collimator itself.

Laser safety is always a priority and the power of the laser can be quite high, in the tens of mW. Therefore the laser falls in the laser safety class 3B, or medium eye hazard. As a safety measure, we do not exceed the 50% laser power, which corresponds to powers below 30 mW (see section QE viewport transmittance). At this power we already observe sufficient photocurrent for determination of the QE. The usage of a collimator results in a smaller, more powerful laser beam. We use laser safety glasses whilst working with the laser and close the curtains around the LEEM during QE measurements. Finally, the QE is mounted in a relatively safe place on the LEEM, whereby any reflected photons from the viewport travel back into the top corner of the room, out of reach for any people working on the LEEM. The viewport shutters do need to be closed during measurements, however, as the light does reflect strongly within the prep chamber.

3.4.2 Calibration

As of now, we are not certain that the detection efficiency of the current QE measurement setup is at 100%. We have yet to determine the optimal geometric configuration of its components. In particular, the distance between the cathode and anode can significantly impact the measured photocurrent. Even a one-centimeter variation can cause a substantial change in the photocurrent, potentially leading to differences of several orders of magnitude, especially with just a 40V potential difference. A distance sweep would therefore be insightful, with voltage and laser power kept constant, to fully understand this effect.

An equally important factor affecting QE is the voltage applied between the cathode and anode. In the current setup, the cathode (the photocathode) is grounded, while the anode

is held at +40V, which is the maximum output of the Keithley 2450. It remains uncertain whether the photocurrent has saturated at this voltage or whether a higher voltage could release additional photoelectrons, increasing the measured QE. As the current QE is likely a minimum value, further measurements should be conducted by carrying out a voltage sweep, preferably from 0V to 40V in 1V increments, whilst maintaining a constant laser power and cathode-anode distance. This would allow us to assess the slope of the photocurrent, and thus the QE, as a function of voltage, and help identify at what voltage saturation appears. It is worth noting that the current setup is designed for low voltages, where 40V may already be at its upper limit. Although the electrical feedthrough (yellow flange on top, Fig. 3.1C) can sustain up to 500V/5A per pin, the limiting factor might be the voltage tolerance of the thin in-vacuum wires.

These two sweeps need yet to be carried out and by combining their results we can evaluate the impact of both distance and voltage on the measured photocurrent and thus the computed quantum efficiency. We can then determine the optimal arrangement of the anode in our setup.

A major component of the QE work that was in fact carried out involved expanding the pre-existing code, as the experimental setup was largely complete. The FISBA laser can emit at three different wavelengths, all of which are relevant for QE measurements. We cycle the laser through 450 nm (blue), 520 nm (green), 660 nm (red), and an 'off' state for background measurement. This allows us to compare the QE at different wavelengths under similar conditions, as the photocathode growth process is typically slow enough for meaningful comparisons. This four stage cycle takes approximately 12 seconds to complete and is repeated indefinitely unless specified otherwise. However, this approach was only implemented during the later stages of the research, meaning some of the figures in this thesis present QE data for only one wavelength.

In addition, an issue with the initial few photocurrent data points became apparent during measurements. The system behaves like a capacitor, requiring time to charge up to 40V. During this brief charging period, the Keithley instrument was already logging current, which resulted in notably low initial readings. This issue was identified late in the research, after which the code was modified to first stabilize the system at 40V before commencing measurements.

3.4.3 QE viewport transmittance

Another important aspect of the calibration for the QE measurements is the consideration of the silica viewport located between the vacuum and the laser. Reflection and absorption lead to a lower transmittance of the laser light towards the photocathode, how much depends on the laser power and wavelength of the light. We assume the transmittance to be a constant once measured, although this may not be the case. Since we evaporate, it is possible that slowly a thin layer of Cs and Sb accumulates on the viewport. However, we expect this process to be negligible, as the viewport is located besides the DCS evaporator. This means that mainly the other side of the preparation chamber is coated by Cs and Sb during evaporation. A small portion of the atoms may reflect back on precisely the viewport. Yet, we cannot see any such deposition by eye after at least three months of evaporation.

The transmittance of the specific viewport has been measured once by hand, by removing it from the chamber and placing it down on an optical table. The laser was also screwed into the same optical table and aligned with a pyroelectric energy sensor (ES254C Thorlabs) placed behind the viewport. The sensor is able to measure the laser power with an accuracy

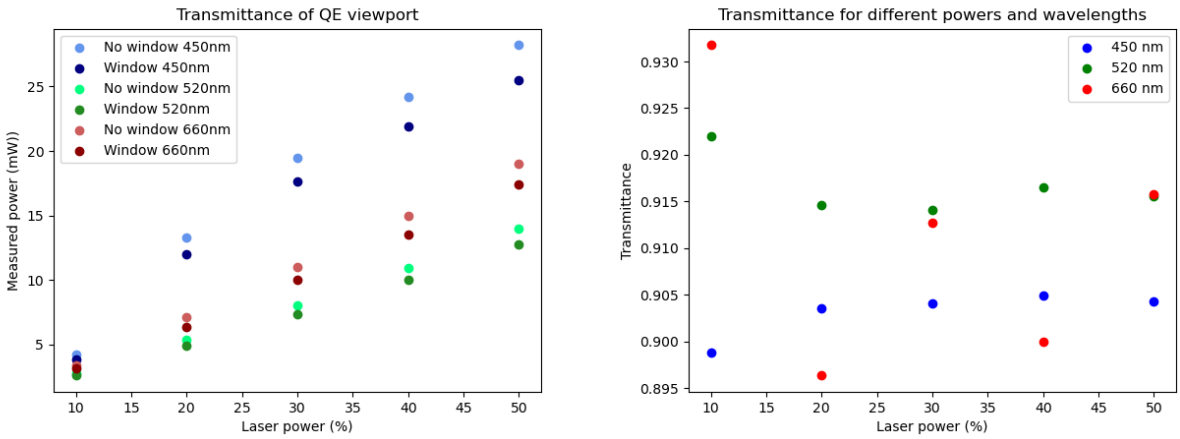

(A) **(B)**

Figure 3.8: *Transmittance of the laser power in absolute and percentual values of the laser light through the UHV viewport.* **(A)** *The transmittance of the viewport through which the laser for the QE setup emits. It is measured also without a window to compare the amount of loss, which differs per wavelength and output power.* **(B)** *Percentual transmittance due to viewport absorbance and reflectivity in laser power.*

of two decimals in the mW range and is connected by cable to a small screen, from which the results can be read out manually. The measurements were carried out in steps of 10% of the laser power, from 10% to 50%, as the power output differs per wavelength. We did not use a power higher than 50%, as this is already quite harmful to the naked eye and a photocurrent was easily measurable above noise levels for the average photocathode. The same measurement was carried out with and without the viewport located in between the laser and sensor and the results are plotted in Figure 3.8A.

The sensor showed a small but notable loss in transmitted laser power when the viewport was placed in between. For a 10% power setting, all values lie very closely together, around the 4 mW in measured power (Fig. 3.8A). It should also be noted that the laser power of the 660 nm light is higher than that of the 520 nm light when set at the same percentage, although the photons of the 520 nm light carry more energy. This is simply a property of the laser, but can seem counterintuitive in the figure. The absolute loss increases with the laser power and Figure 3.8B shows us that the transmittance, or the conversely related percentual loss is actually quite constant at different powers. This should indeed be true as the transmittance should be power independent, provided that the viewport remains unaffected. Specifically blue and green light seems quite stable, whereas red fluctuates somewhat more. The losses for all three wavelengths for all laser powers lie around the 9%, i.e. circa a transmittance T of 91%. This is consistent with the specs of the HOVPZ38LAQ flange made out of fused silica*. The decrease of the transmittance of red light does however seem to be plausible given Figure 3.8A.

All in all, to calculate a quantum efficiency closer to the actual internal QE of the photocathode one should use these calibrated power outputs of the laser. The QE is then calculated through Equation (2.3), using the actual transmitted laser power for P.

As only powers up to 50% laser power were measured in this research, a linear fit was performed on the data to predict what higher laser percentages would represent in laser power.

*https://www.hositrad.com/cf-flanges/viewports/zero-length/viewport-zero-length-cf-fused-silica-braze.html

The fits were carried out both with and without the first datapoints for all wavelengths and the linear fit for the 450 nm light was quite imprecise with this first datapoint. The datapoints for all three wavelengths of the 10% laser power all lie close together and it seems that the laser is not yet operating properly at this low power level. This is directly visible in the data beyond that, as here the datapoints for the three colors aren't grouped together at all. Omitting this increased the R^2 value of the fit (see Table 3.1) and it was also clearly more accurate when visualized. The fit equations were then used for extrapolation of the laser power at higher laser power percentages.

Measurement	All slope	W/o dp1 slope	All R^2	W/o dp1 R^2	Linear fit	*T*
450nm No W	0.588	0.495	0.972	0.990	y = 0.50x + 3.97	
450nm W	0.533	0.448	0.972	0.990	y = 0.49x + 3.58	0.904
520nm No W	0.278	0.286	0.999	0.999	y = 0.29x + -0.45	
520nm W	0.255	0.263	0.998	0.999	y = 0.26x + -0.43	0.915
660nm No W	0.391	0.396	1.00	1.00	y = 0.40x + -0.82	
660nm W	0.356	0.365	0.999	1.00	y = 0.37x + -0.93	0.906

Table 3.1: *The linear fit data of the QE viewport measurements. In the measurement column, W stands for window. The second column represents the slope of the fit on all the data, whereas the third column denotes the slope when the first datapoint is omitted (without datapoint 1). The All R^2 and W/o dp1 R^2 columns state the R^2 of the fit, i.e., the goodness of fit, which is clearly higher when omitting the first datapoint, specifically for 450 nm. Finally, the last two columns represent the linear fit equation that can be used for the extrapolation and the transmittance T values, which are similar for the three wavelengths.*

According to the supplier, the maximum output powers for each wavelength respectively are 40 mW for 450 nm and 660 nm and 30 mW for 520 nm. The extrapolation of the data in Figure 3.8A, however, yields a value of 48 mW for 450 nm light at 100% laser power. Thus, in a QE measurement using 100% laser power with 450 nm light, the actual laser power should be roughly a factor 0.8 of the extrapolated value, namely 40 mW instead of 48 mW. This means that the QE should in fact be a factor 1.25 higher than calculated. Although, it is plausible that the laser performs better than specified.

A simple solution to this issue would be to carry out a laser power measurement sweep across all laser power percentages for all three wavelengths and to use this as reference for the QE calculation. This can be easily carried out in following research.

3.5 Transfer arm extension

3.5.1 Practical

Preferably, if all the evaporation goes well, we would like to grow not just a polycrystalline photocathode and measure the QE, but actually grow the Cs_3Sb cathode in an epitaxial manner. This means that the deposited layer is at least correlated to the crystal structure of the substrate on which it grows and that the layer has minimal defects. The latter may be of importance for the QE yield. This crystallization occurs at sample temperatures of approximately 80 °C [7]. Clearly, we need a heater that can keep the sample at stable temperature, in UHV. We opted to design and fabricate our own heater in collaboration with the FMD and the Electronics Department (ELD). This heater needed to fit on an extension of the new horizontal that is positioned opposite of the DCS, such that the sample receives the evapo-

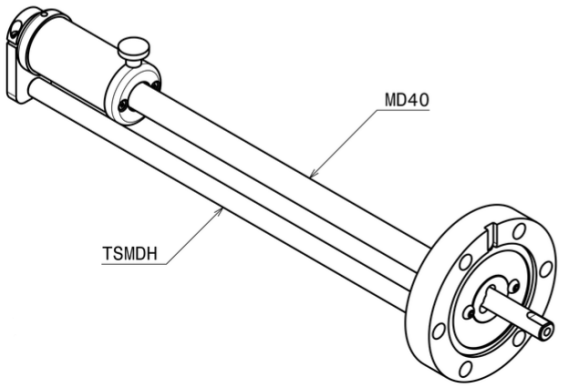

Figure 3.9: *The transfer arm with a CF40 flange and 100 mm reach. An extension was later connected onto its in-vacuum part, on the right-most side of the arm after the flange.*

rant head on. As we want to monitor and control the sample temperature, we also need to install a thermocouple on this extension which is in good thermal contact with the sample.

The transfer arm that was bought for this research is the Linear-Rotary Feedthrough from UHV Store of Switzerland, with a CF40 flange and a linear travel or reach of 100 mm (Fig. 3.9). The latter became important, as there was little space available where the transfer arm is mounted. More reach also means a longer out-vacuum part of the transfer arm, which would come to interfere with the EDX setup. Furthermore, we placed a new port aligner between the LEEM and the transfer arm that gives us the ability to slightly redirect the transfer arm, which is very useful and perhaps even necessary during transfer of the sample as the transfer arm doesn't line up perfectly with the samples in the vertical transfer arm. This port aligner adds another 7 cm to outside length of the transfer arm. The current transfer arm setup consequently has just a few cm leeway with the EDX.

For our measurements, we also need a ground connection to the sample, grounded with respect to the chamber and therefore the anode of the QE circuit. Here, we were able to repurpose the ground cable from the existing in-vacuum QE setup. Overall, for our new transfer arm we required a heater, a thermocouple and a ground connection. The final transfer arm extension is shown in Figure 3.10A and 3.10B.

The extension consists of three parts. The first part is a small section of stainless steel (grey) which is used to fix the extension onto the transfer arm by screwing it in place. The second and largest part is the MACOR piece (white), which is a trademarked glass-ceramic that is easily machinable, has a high temperature resistance up to 800°C in vacuum, is both a great thermal and electrical insulator and is UHV compatible. Some back-of-the-envelope calculations showed that such a long MACOR part with roughly a 1 cm diameter was sufficient to withstand temperatures of 100°C during several hours of sample heating. The third and final part of the extension is the most complex. Its base is made of copper, which has high thermal conductivity and excellent electrical conductivity. The copper is heated via four 75Ω resistors that are connected in series and are screwed onto the copper. The ground connection for the QE is fixed behind one of the screws of the resistors. The TC that monitors the sample temperature is secured to the head of the copper part with Kapton tape, which is UHV compatible and can withstand temperatures up to 260°C. This TC should be in proper thermal contact with the copper. The TC here is type K and consists of a Nickel-Chromium and a Nickel-Alumel leg and was manually made by the ELD. It is sleeved by a thick UHV compatible glass sleeve, which is the thick white wire in Figure 3.10B. The top of the copper has a screw thread and is specifically altered to accommodate a tantalum spring with which

(A) **(B)**

Figure 3.10: *The custom transfer arm extension made in collaboration with the FMD and ELD.* **(A)** *Before wiring, but with the heating resistors screwed on.* **(B)** *Transfer arm after wiring of heating element, ground and TC.*

the sample cap is handled during transfer. The actual sample temperature will probably be lower than as indicated by the TC, as it is yet to be determined how well this spring thermalizes with the copper. It is yet unclear how long this would take and if the surface area of contact between the two parts can be increased to speed up the thermalisation.

We have also secured Kapton tape on many places on the copper where possible shorting could occur, such as between the wires delivering the current to the resistors and the copper surface closely below it. Finally, after the resistors, ground connection and TC were fixed in place, everything was connected and led along the MACOR away from the copper. The connections were made via the in-vacuum cables that belong to the electrical feedthrough on top of the prep chamber (yellow flange in Fig. 3.1C). This feedthrough has nine pins of which we have used six: two for the heater power, two for the TC and two for the QE system. A custom cable was assembled by the FMD for the out of vacuum connection, which contained six wires for all the pins bundled into one large cable. This cable culminated into the six wires which were connected to a power source (heater), the OMNI controller (TC) and the Keithley 2450 (QE).

3.5.2 Calibration

The new transfer arm was installed briefly before the end of this research and there was not enough time to do the full calibration measurements. We did, however, connect the TC to the OMNI controller which did show a temperature of 24°C before heating, which roughly complies with room temperature. Furthermore, we used the same PSU for sample heating as for the DCS, which could maximally supply 31V with 0.09A. The heating power is thus circa 2.8W, which is still considered safe and sufficient for our system, as we initially aimed at a 1W or 2W heating power. During the first heating test the temperature stabilized at 77°C after 50 minutes of constant heating and was heavily outgassing, as the pressure in the prep chamber went from $4 \cdot 10^{-7}$ mbar up to $1.4 \cdot 10^{-6}$ mbar. We subsequently carried out a bake-out of the prep chamber over the weekend. After the weekend, the sample heater was turned on again and achieved a maximum temperature of 82°C at a pressure of $8 \cdot 10^{-7}$ mbar.

Figure 3.11: *The transfer arm extension installed inside the prep chamber.*

Again, the desired goal here would be to combine all the scripts such that during measurements the live data can be shown of the photocurrent/QE, the evaporation rate, the layer thickness, the pressure, the Cs and Sb crucible temperatures and the sample temperature.

3.6 Substrate preparation

First, a square piece of silicon (Si100) is cut to the appropriate size to fit in a LEEM sample cap. The substrate is then cleaned to remove any organic contaminants by sequentially submerging it in acetone and IPA. After the chemical cleaning, the substrate is placed in an ultrasonic bath for several minutes to dislodge any persistent contamination. Once the sonication is complete, the substrate is dried with gaseous nitrogen and placed into the sample cap, where it is locked in place by a small spring behind it. The sample cap is then ready to be placed into the LEEM loadlock.

ONEM substrates are required to be electron transparent for the photoelectrons from the photocathode to get into the LEEM. These substrates can be a layer of graphene or a silicon nitride membrane. These ultra-thin substrates require to be handled more delicately than the Si-100 substrates and often are taken clean directly from the supplier.

Chapter 4

Results & Discussion

A major part of this research consisted of the designing, installing and calibrating the DCS, QCM, QE and transfer arm. This process contained many results in itself and these are readily discussed in chapter three. In this chapter, we will discuss several samples for which we also have LEEM, LEED and EDX data. Together, this data provides a more clear overview of the quality of the photocathodes that were grown on these particular substrates.

4.1 Measurements

It should be noted again that the layer thicknesses in the data are reported by the QCM. However, this value has not yet been calibrated through some tooling factor with the actual thickness of the photocathode, which could differ notably. Nevertheless, the reported QCM thickness can already be used as a measure for comparison of the different samples.

Furthermore, the colors in the QE plots correspond to their respective wavelengths, i.e. 450 nm, 520 and 660 nm laser light data is represented by the blue, green and red datapoints respectively.

Finally, since the edges of the LEEM field of view often display irregular behavior, the WF is computed only within a large square ROI (red square) of the image. This ROI is divided into squares of 4x4 pixels, each of which is processed individually during the computation of the WF via the error function fit (as described in Equation (2.2)) applied to the IV curve. The LEEM image shown is of an arbitrary frame during the IV sweep. Additionally, the WFs have been calibrated relative to the substrate, which has a WF of approximately 5.0 eV, as mentioned in section *LEEM work function analysis*.

4.1.1 Sample 129/run 19

The photocathode of sample 129 was created during an early run in the measurement time and is here used as an example for the WF determination. The grown layer was 10 nm thick according to the QCM. Its computed average WF is -1.27 eV (Fig. 4.1C) with respect to the substrate WF. This translates to approximately WF = 3.7 eV. This would mean that this photocathode was of inferior quality, yet the WF was actually reduced. A high quality Cs_3Sb photocathode would have a WF closer to 2 eV. The WF of pure Sb is around the 4.5 eV. This indicates that the Cs rate during this rate was presumably too low and thus the Cs:Sb stoichiometry ratio of the photocathode was notably below 3:1. Also, there is a small

Version of October 30, 2024– Created October 30, 2024 - 11:40

local maximum after the transition, which is indicative of the internal band structure of the photocathode.

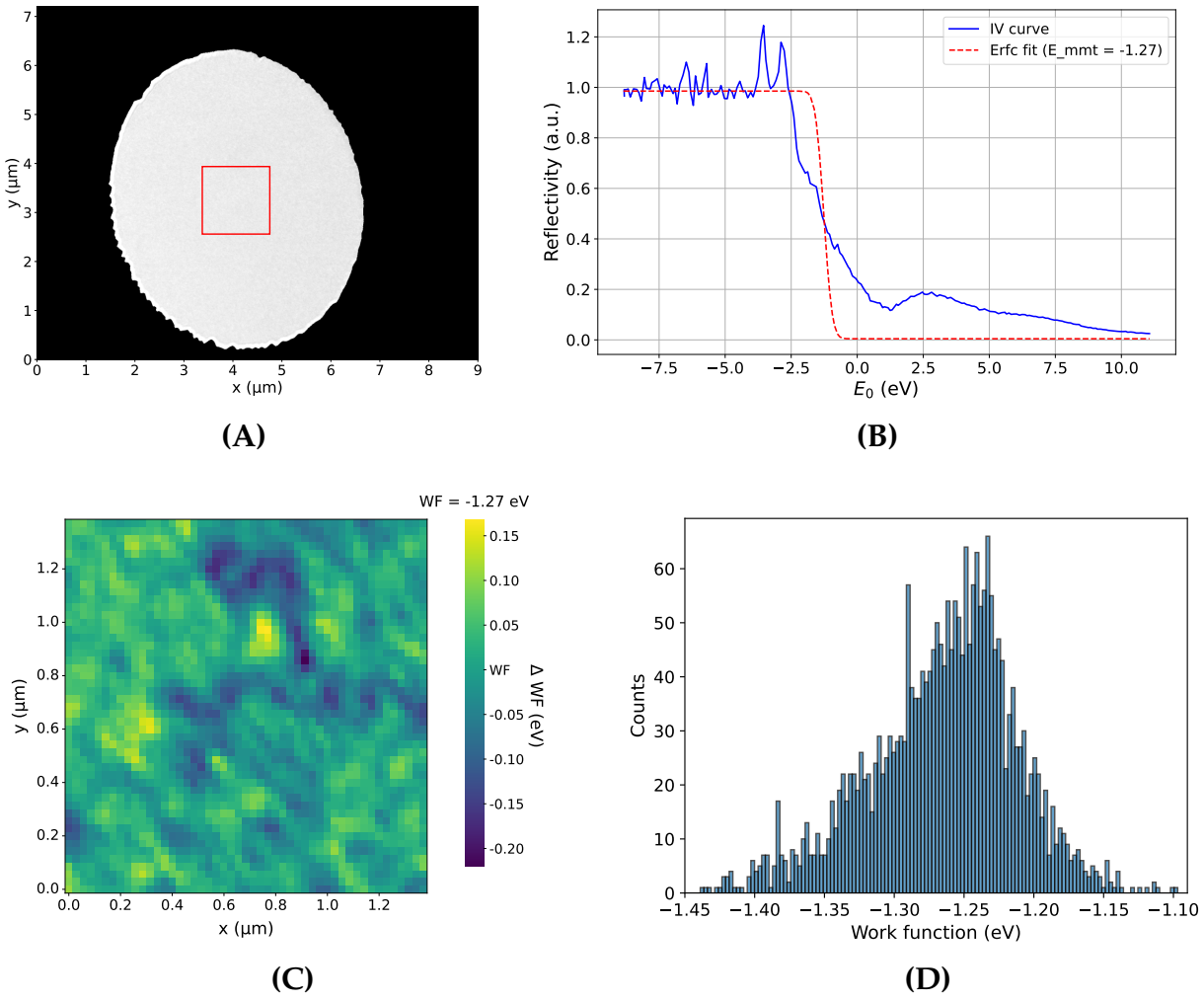

Figure 4.1: *LEEM data of sample 129. The WF is normalized to the substrate.* **(A)** *ROI of the photocathode.* **(B)** *Erfc fit to the average IV curve of all squares within the ROI.* **(C)** *Heatmap of normalized WFs in the ROI.* **(D)** *Histogram of the work functions inside the ROI.*

In addition to the heatmap, the corresponding distribution of the WFs in the heatmap is given in Figure 4.1D. The distribution peaks at circa -1.24 eV and is somewhat left-skewed. Its FWHM is estimated at 120 meV and the heatmap reveals a blend of lower and higher WF areas. These are quite different compared to the WF fluctuations of sample 125 (Fig. 2.2C) as those were very localized (impurities). Here, the heatmap indicates more of a regional fluctuation, which do differ on the same order as of sample 125 at roughly $\pm$ 0.2 eV.

4.1.2 Sample 135/run 31

Run 31 was the first run of which the QE was logged. The evaporation rate was very stable as shown by the constant slope of the thickness (Fig. 4.2). The QE started out relatively high already at circa 1 nm thickness and increased to 0.3% at 10 nm thickness. We do see that the slope of the QE started decreasing after the photocathode reached circa 5 nm thickness.

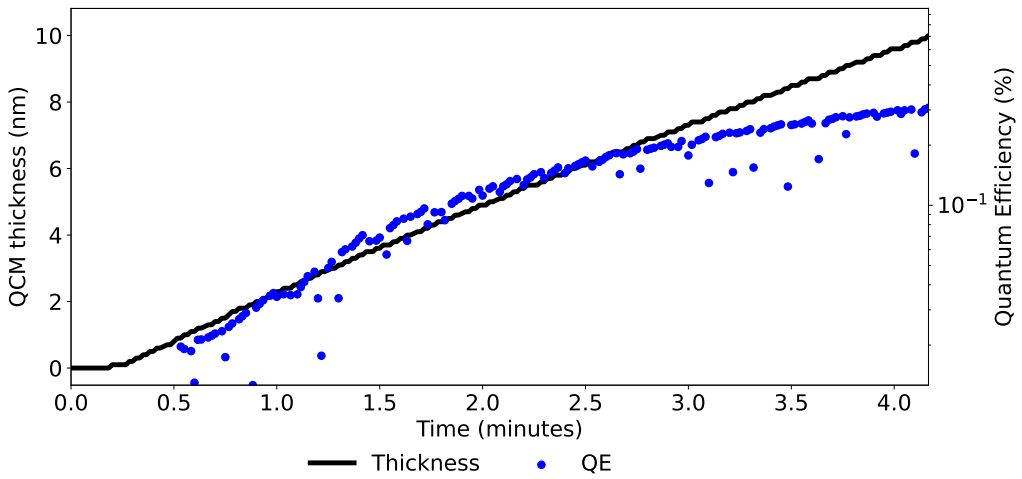

Figure 4.2: *Run 31 QE and QCM overview.*

4.1.3 Sample 136/run 33

This photocathode was grown to 30 nm and exhibited quite a low QE, of the order of 10^{-4} %. The QE was measured over almost a two hour period until the QE software unfortunately crashed (Fig. 4.3). There is a clear decline in QE over time, although it is hard to conclude that the degradation over time is significant, as the QE itself is very low. A higher QE photocathode could perhaps be more stable over a similar period of time. No definitive conclusions can be made from this stand alone measurement. The decline in QE can be explained by desorption of Cs over time, which lowers the QE. This means that the stoichiometry was already below 3:1, as this desorption led to an even lower Cs:Sb ratio.

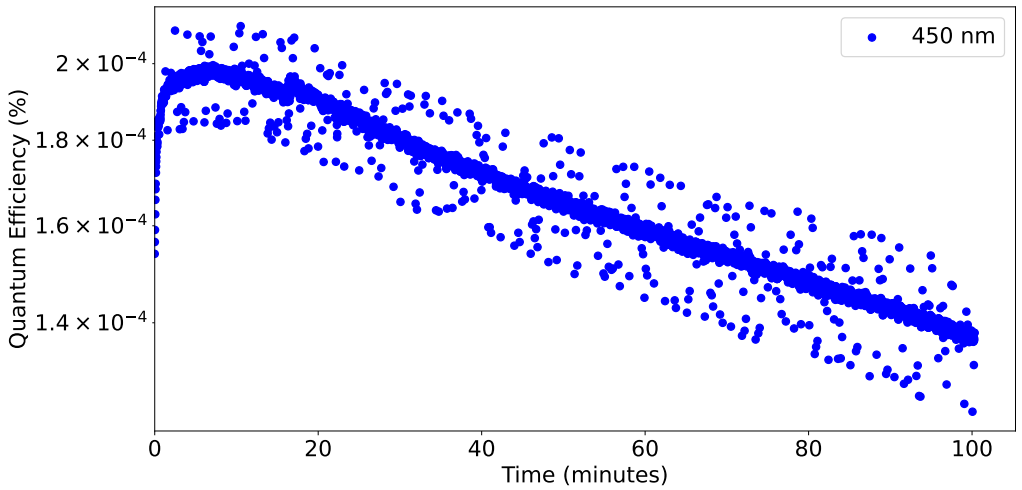

Figure 4.3: *Run 33 overnight QE and QCM overview.*

4.1.4 Sample 139/run 36

This was the final photocathode grown during this research. In this run, we more clearly documented the opening and closing of the Cs and Sb shutters, as shown by the grey areas in Figure 4.4. The layer was grown to approximately 40 nm in about 16 minutes, during which the sample heater was turned off. The slope of the thickness graph indicates a higher growth rate at the beginning of the run, which then gradually decreased. The evaporation rate and QE are very alike during the first co-evaporation period until just after the six

Version of October 30, 2024– Created October 30, 2024 - 11:40

minute mark and during the Sb-only period directly after it. We concluded that there was actually very little Cs being evaporated and subsequently increased the Cs crucible current.

This did in fact increase the QE during the second co-evaporation period that starts around the nine minute mark. Then, the photocathode was cesiated and an approximately 5 nm layer of Cs was deposited on top of the already very thick layer of Sb. This is the reason that the QE spiked upwards, peaking just below 10^{-3} %. However, the Cs will subsequently diffuse further into the Sb layer to form a cathode [7]. Yet, with the amount of Sb deposited here the Cs was not nearly sufficient to form a fully well-working photocathode. Thus, it is likely that the QE decreased again because of diffusion of Cs in the top layer of the cathode into the bulk below.

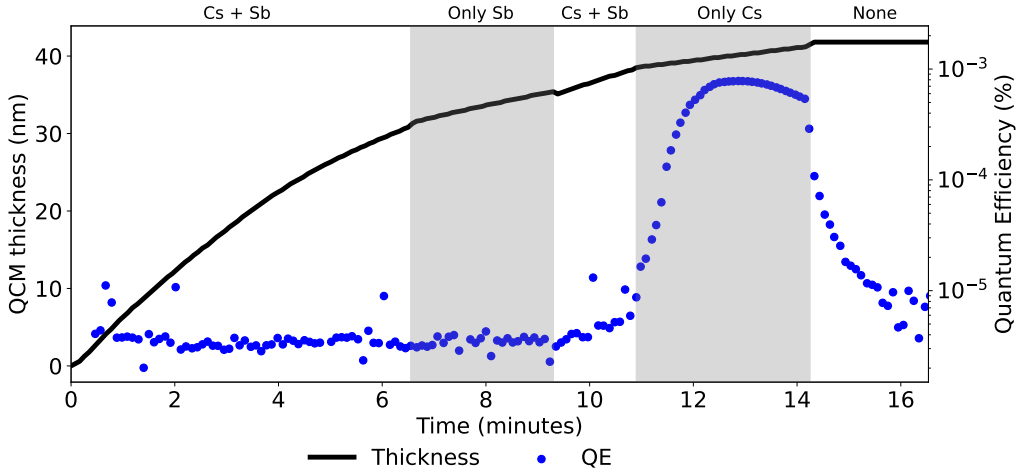

Figure 4.4: *Run 36 QE and QCM overview.*

The resulting heatmap of the photocathode surface within the ROI is shown in Figure 4.5C. Notably, this photocathode demonstrates a high degree of homogeneity in WF across its surface, with the colorbar indicating a maximum deviation from the average WF of circa 25 meV. The average WF for this ROI is 0.18 eV with respect the reference sample (sample 125 in section *LEEM work function analysis*). Thus, this computed WF is actually higher than that of the substrate itself. This could be explained by the likely inferior composition of the grown photocathode. The immediate decrease of QE after the cesiation stops is an indication of this poor quality. It could be that we have depleted the Cs crucible during this evaporation run and have consequently deposited some undesired contaminants onto the substrate. We hypothesize that this sample consists of a thick Sb layer with an oxidized top layer and little Cs. Such an oxide layer would explain the smooth WF we observe here.

The distribution of the WFs is illustrated in Figure 4.5D and shows a roughly Gaussian shape. Its peak lies close to 0.18 eV and has an estimated FWHM of 25 meV. We are supposedly mostly observing a Sb surface here.

Interestingly, a slight gradient is shown in the heatmap (Fig. 4.5C), whereas we indeed expect a homogeneous Sb layer. We suspect that this gradient is due to a small tilt of the sample and a defocused electron beam (Fig. 4.6). Because the electron beam travels slightly uncollimated, a small perpendicular momentum gradient is introduced across the beam. When these electrons then come into the vicinity of the sample, the perpendicular electric field decelerates them equally. Yet, as their perpendicular momentum already differed (orange arrows in Fig. 4.6), the electrons will reach the sample at different stages during the IV sweep. Solely considering defocus, we would expect a gradient in the shape of the electron

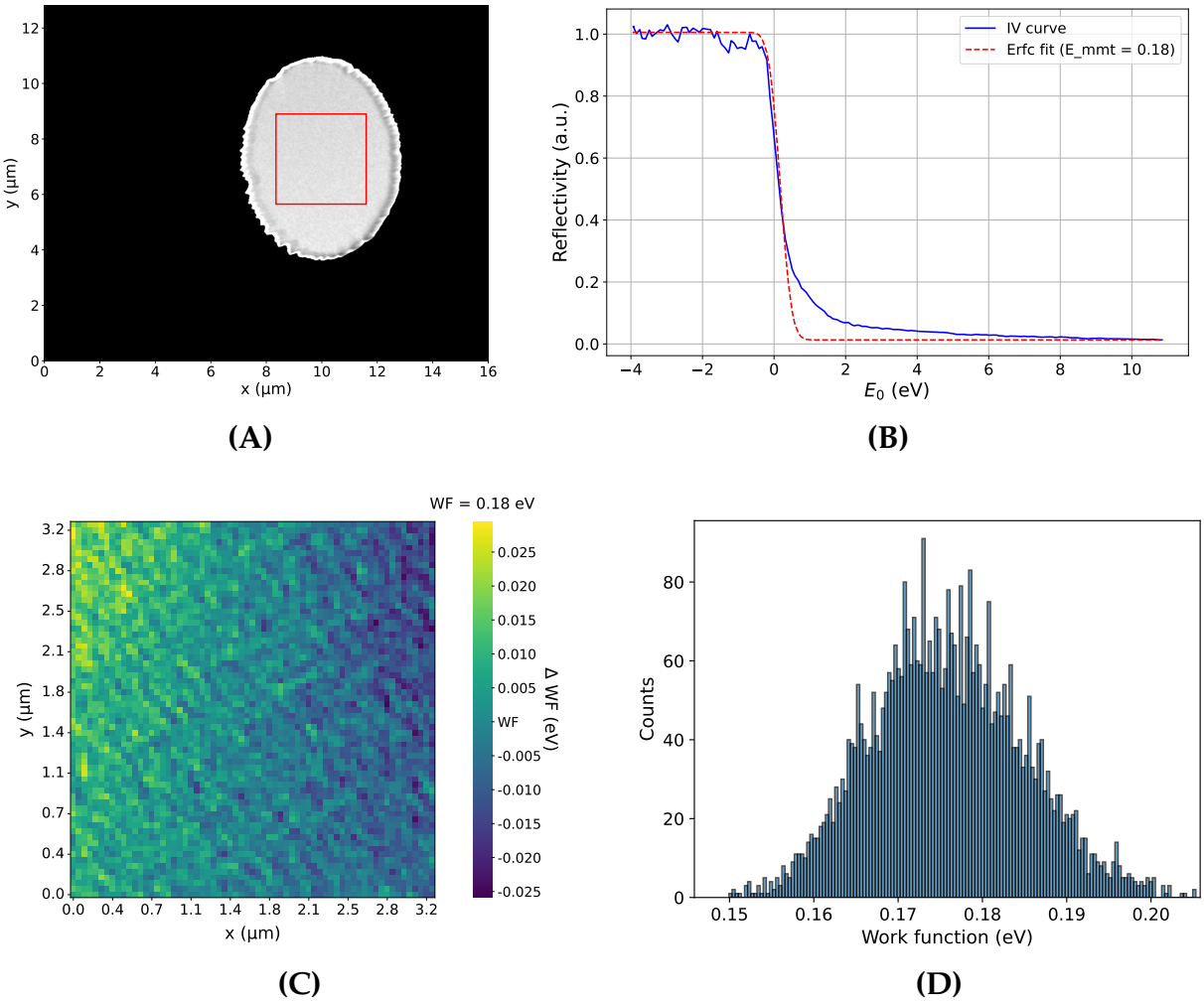

Figure 4.5: *LEEM data of sample 139. The WF is normalized to the substrate.* **(A)** *ROI of the photocathode.* **(B)** *Erfc fit to the average IV curve of all squares within the ROI.* **(C)** *Heatmap of normalized WFs in the ROI.* **(D)** *Histogram of the work functions inside the ROI.*

beam as the electrons on the inside of the beam would have the same perpendicular momentum and would change the MMT equally. As we probe a large section of the beam and we observe only a gradient in one direction, the sample is likely also tilted as the difference in path length for the electrons between either side of the beam results in the observed WF gradient across the sample. Note that the scenario with only a tilt, but a collimated beam, yields a certain momentum difference similar for all electrons in the beam and thus no WF gradient. Therefore, this gradient is likely the result of the combined effect of sample tilt and an uncollimated beam.

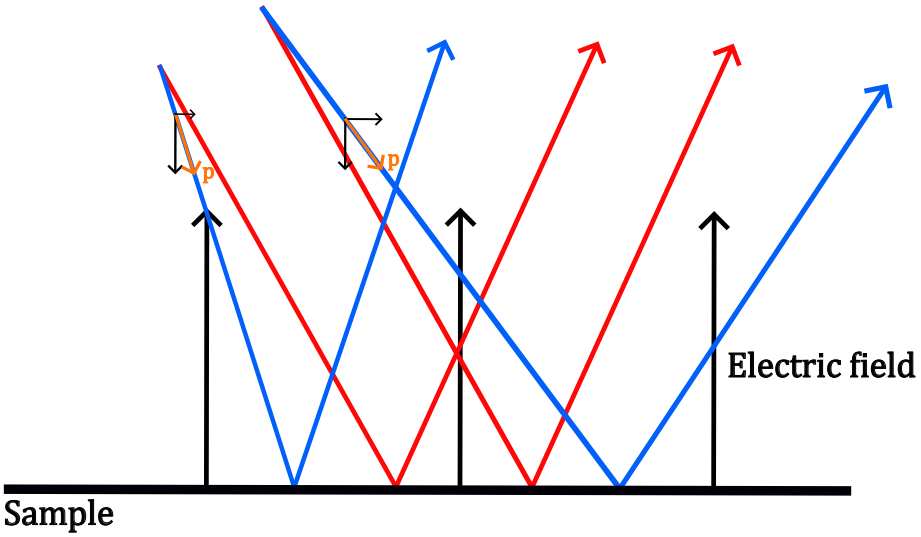

Figure 4.6: *In red, a collimated electron beam reflects onto a tilted sample. In blue, a defocused electron beam reflects on the same tilted sample. Electrons in some part of the defocused beam have more perpendicular momentum than others, as is shown via the decomposition of the small orange momentum vectors* ***p****. Here, the right electron has more horizontal momentum and the left electron more perpendicular momentum.*

4.1.5 Sample 148/run 38 & 40

At the end of this project, the prep chamber setup was used to grow a Cs_3Sb photocathode on a biological sample, marking the first serious attempt at ONEM with the new type of photocathode. The biological sample consists of a 40 nm slice of mouse brain tissue placed on an ITO-coated fused silica substrate.

Two separate Cs_3Sb growths were performed, since during the first run (run 38) the sample was apparently flipped and a layer was deposited on the sample's fused silica backside. The photocathode that was grown showed a subpar QE performance as the maximum lied around the $7 \cdot 10^{-3}$ % for 450 nm light (Fig. 4.7A). The QE for all three wavelengths roughly plateaued at a thickness of 4 nm, when the Sb shutter was closed. Then, only evaporating Cs, the QE was still slightly increasing until the moment both shutters were closed around the 36 minute mark. The final cesiation period was carried out to improve the stoichiometry to a be closer to 3:1, as we expected the photocathode to be under-cesiated. Finally, the photocathode reached a 8 nm thickness.

After discovering the incorrect sample orientation, the sample was flipped, and evaporation run 40 was initiated. Once again, an 8 nm photocathode was deposited on the sample. This time, the QE plateaued at a thickness of approximately 6 nm, again the moment when the Sb shutter was closed (see Fig. 4.7B). The QE showed a slight increase during cesiation between 6 and 8 nm, with a maximum QE for blue light reaching about 0.3%. This indicated that the photocathode was of modest quality and suitable for ONEM imaging.

In fact, this was the attempt with which the first ONEM image could successfully be produced using a photocathode grown in the preparation chamber of the ESCHER LEEM, fulfilling one of the primary goals of the project beyond engineering and calibration. Figure 4.8 displays one of the ONEM images of mouse brain tissue captured during this experiment. Although the resolution was not ideal, several structural details are already apparent such as the large black closed loops. These loops are myelinated axons, part of the neurons, and are clearly distinguishable [21].

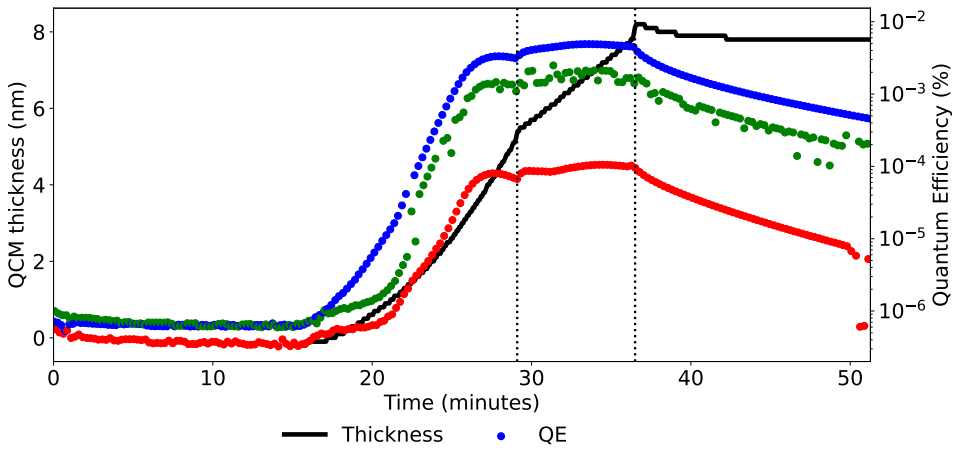

(A)

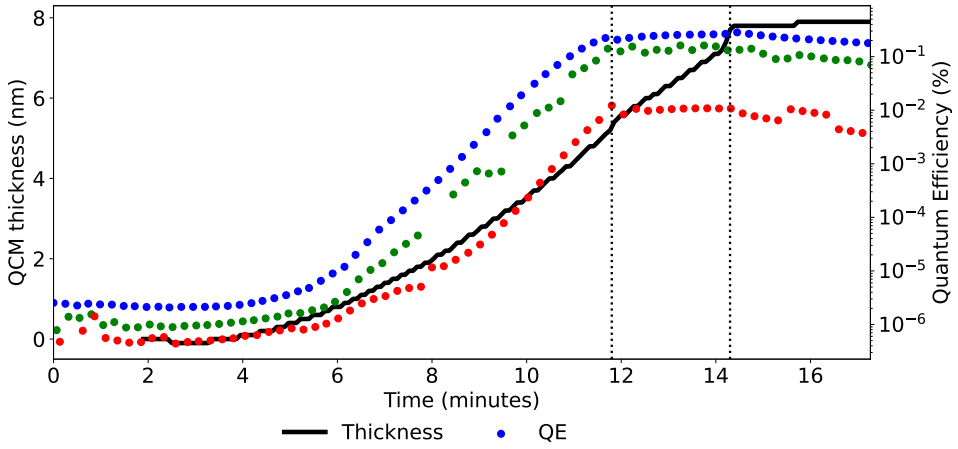

(B)

Figure 4.7: *QCM and QE data during two evaporation runs on a mouse brain tissue sample on both sides of the substrate. Dotted vertical lines indicate shutter closure. For both plots the left one is the Sb shutter, and the right Cs.* **(A)** *and* **(B)** *represent run 38 on the backside of the substrate and run 40 on the front side respectively.*

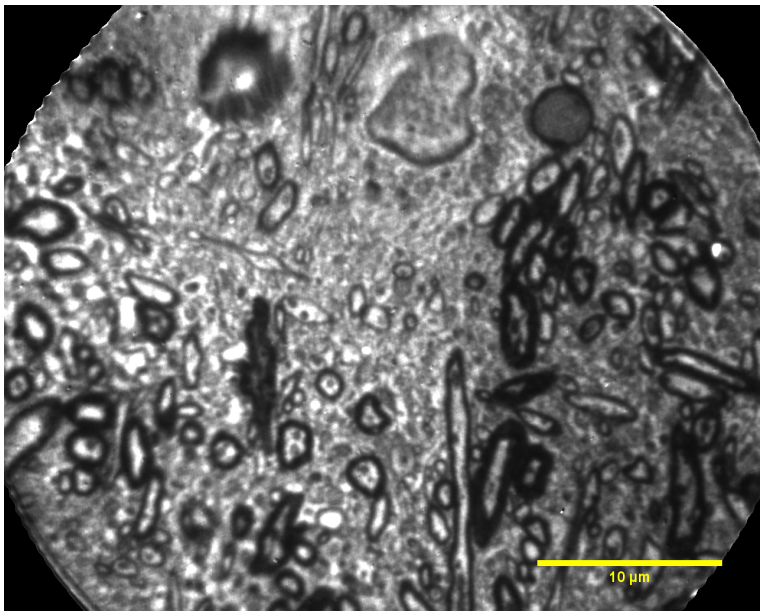

Figure 4.8: *ONEM image of mouse brain tissue, 45* µm *FOV. Here, the large black closed loops are myelinated axons.*

Version of October 30, 2024– Created October 30, 2024 - 11:40

Chapter 5

Conclusion & Outlook

This research targeted the development of Cs_3Sb photocathodes for Optical Near-field Electron Microscopy (ONEM), focusing on their controlled *in situ* growth and performance optimization inside the preparation chamber of the ESCHER LEEM. The primary objective was to produce ultra-smooth, ultra-thin photocathodes with high quantum efficiency (QE) that could effectively realize ONEM. To this end, a major part of the project was to design and carry out a plan for the arrangement of the components that were needed to reach this goal.

We have used a Dual Cluster Source (DCS) evaporator for co-deposition of Cs and Sb, a Quartz Crystal Monitor (QCM) to monitor the evaporation rate and the photocathode thickness during evaporation and a quantum efficiency (QE) setup containing an *in situ* anode to collect excited photoelectrons by the QE laser. Lastly, we've designed and engineered a custom transfer arm extension for the new transfer arm we use during deposition. This arm contains an electrical ground for the QE circuit and a custom-built heater consisting of heating resistors to heat the sample during deposition to realize crystallization of the photocathode.

During this research many photocathodes were grown with differing evaporation rate ratios and thicknesses on silicon-oxide (Si-100) substrates. Here, the general target stoichiometry for the photocathodes and thus the evaporation rates was 3:1. Few photocathodes exhibited moderate yet feasible QE values around the 0.3% for 450 nm laser light. This was in fact sufficient for ONEM imaging of a biological sample, yielding modest resolution and intensity. This demonstrates the potential of the preparation chamber additions.

Nevertheless, this research is only the start of the work on the preparation chamber. Most physical components are in place, yet many aspects of the data-analysis and live data visualization need to be streamlined. The temperature logging of the thermocouples of the DCS crucibles and the transfer arm heater needs to be finalized. When all this data is available, it would be easier to implement for example a PID system to control the evaporation rate through altering the current led into the DCS in real-time. Then, ideally all live data could be unified into one interface. While the current system was evidently functional, such integration would provide smoother and a more consistent and reproducible method for photocathode growth.

An updated visualization for the evaporation rate would make it possible to use even lower rates, as now the noise levels where too high to state these rates accurately by eye. A lower rate would result in slower depletion of the Cs. This was a slight issue during this research as it meant a frequent Cs refill was needed. This meant that the preparation chamber needed

Version of October 30, 2024– Created October 30, 2024 - 11:40

to be vented which resulted in extra downtime of the photocathode growth experiments and in subsequent outgassing of the Cs and Sb.

Furthermore, the heatmap creation of the photocathode work function should be optimized. For now, the analysis incorporated 4x4 pixel squares, for each of which an error function was fitted to its IV curve to obtain the work function. This should be altered to a pixel-by-pixel analysis within some predefined ROI for optimal resolution. However, this would require more powerful computational resources, as the current system was limited by processing speed. Improving the speed and accuracy of these measurements would not only enhance the characterization of photocathodes but also inform better growth control for future experiments.

Another promising direction for future research is the use of advanced band structure analysis techniques, such as Angle-Resolved Reflection Electron Spectroscopy (ARRES). This method would allow for a detailed understanding of the conduction band, which is crucial for optimizing the photocathode's electron emission properties. By mapping the band structure, researchers can better understand how this influences the photocathodes's QE and MTE.

Ultimately, this research has successfully demonstrated the feasibility of growing Cs3Sb photocathodes for ONEM, with moderate QE levels that are sufficient for imaging applications. However, there is room for improvement in both the deposition process and the resulting photocathode performance. The suggested improvements could possibly enhance the effectiveness of ONEM photocathodes, facilitating broader applications in high-resolution, non-invasive microscopy.

Version of October 30, 2024– Created October 30, 2024 - 11:40

Acknowledgements

I have really enjoyed my time here in the van der Molen group at Leiden University. During the last few months I have learned many engineering skills, which I did not really possess beforehand as I am typically more theoretically minded. As always, I must thank my beloved girlfriend Serafine. She has yet again reviewed my thesis thoroughly, as is tradition by now.

Furthermore, I have enjoyed many great moments with my project partner, Dalal, whom I already had the pleasure to *endure* during our previous master's research project. Thank you for the daily chats and the intensive collaboration. We clearly loved talking to the customer services of the several suppliers we contacted and hearing back that our desired part had a delivery time of 28 weeks. As such, we had to adapt and make some compromises. Overall, however, I think we did well.

As my daily supervisor, Guido has learned me many things about the LEEM and the corresponding physics. I really enjoyed talking to him on a daily basis about this in an always relaxed and friendly atmosphere. The several times we opened the prep chamber (hours of work) were great bonding experiences. Although, I would rather forget how many times I have dropped a wrench, nut or bolt in a very inconvenient place between the cabling and machinery of the LEEM. I got them back every time though! (99% of the time).

I am also very thankful for Peter, who has assisted Dalal and myself many times and operated as daily supervisor if Guido was unavailable. I even witnessed you earning your doctorate! This was the very first PhD defense I attended, which made it all the more special for me.

In the first year of my master here in Leiden I followed the course Condensed Matter Physics, which was taught by Sense Jan. I was immediately sold on the interesting quantum mechanics, the reason why I had chosen this master. I am therefore very glad that I was able to finish my master by carrying out my research project in his group. His warm attitude made me certainly feel welcome in the group and we were also able to have conversations outside of my project. I recall the time we bonded over our shared love for football, which you sadly didn't share with anyone else in the group. I also happily recall our tennis match during the LION sport day. Those personal connections make it so that these months at the university felt as more than just carrying out a project.

Finally, I must also thank the technicians from the FMD and the ELD. Ruud van Egmond and Christiaan Pen from the FMD have been very helpful as we had to carry out many engineering tasks for our project, such as the transfer arm extension (!). Additionally, I must thank Peter van Veldhuizen and Raymond Koehler from the ELD have helped us fabricate the electronics for the heater on the transfer arm extension. This was no trivial task at all and I was happy to report that our first design did actually work already.

I reflect on my seven years of studying in Leiden with a mix of fulfillment and melancholy. While I am happy, there is also a tinge of sadness in knowing that my time as a student has come to an end. Yet, I wonder what the future might hold for me.

Bibliography

[1] R. M. Tromp, "Low-energy electron microscopy," *IBM J. Res. Dev.*, vol. 44, no. 4, 503â516, Jul. 2000, ISSN: 0018-8646. DOI: 10.1147/rd.444.0503. [Online]. Available: https://doi.org/10.1147/rd.444.0503.

[2] R. Marchand, R. Šachl, M. Kalbá č, *et al.*, "Optical near-field electron microscopy," *Phys. Rev. Appl.*, vol. 16, p. 014 008, 1 Jul. 2021. DOI: 10.1103/PhysRevApplied.16.014008. [Online]. Available: https://link.aps.org/doi/10.1103/PhysRevApplied.16.014008.

[3] C. T. Parzyck, C. A. Pennington, W. J. I. DeBenedetti, *et al.*, "Atomically smooth films of CsSb: A chemically robust visible light photocathode," *APL Materials*, vol. 11, no. 10, p. 101 125, Oct. 2023, ISSN: 2166-532X. DOI: 10.1063/5.0166334. eprint: https://pubs.aip.org/aip/apm/article-pdf/doi/10.1063/5.0166334/18179608/101125_1_5.0166334.pdf. [Online]. Available: https://doi.org/10.1063/5.0166334.

[4] J. Feng, S. Karkare, J. Nasiatka, S. Schubert, J. Smedley, and H. Padmore, "Near atomically smooth alkali antimonide photocathode thin films," *Journal of Applied Physics*, vol. 121, no. 4, p. 044 904, Jan. 2017, ISSN: 0021-8979. DOI: 10.1063/1.4974363. eprint: https://pubs.aip.org/aip/jap/article-pdf/doi/10.1063/1.4974363/15189726/044904_1_online.pdf. [Online]. Available: https://doi.org/10.1063/1.4974363.

[5] P. Saha, O. Chubenko, G. S. Gevorkyan, *et al.*, "Physically and chemically smooth cesium-antimonide photocathodes on single crystal strontium titanate substrates," *Applied Physics Letters*, vol. 120, no. 19, p. 194 102, May 2022, ISSN: 0003-6951. DOI: 10.1063/5.0088306. eprint: https://pubs.aip.org/aip/apl/article-pdf/doi/10.1063/5.0088306/16481935/194102_1_online.pdf. [Online]. Available: https://doi.org/10.1063/5.0088306.

[6] L. Kalarasse, B. Bennecer, and F. Kalarasse, "Optical properties of the alkali antimonide semiconductors cs3sb, cs2ksb, csk2sb and k3sb," *Journal of Physics and Chemistry of Solids*, vol. 71, no. 3, pp. 314–322, 2010, ISSN: 0022-3697. DOI: https://doi.org/10.1016/j.jpcs.2009.12.083. [Online]. Available: https://www.sciencedirect.com/science/article/pii/S0022369709004363.

[7] W. G. Stam, M. Gaowei, E. M. Echeverria, *et al.*, "Growth of ultra-flat ultra-thin alkali antimonide photocathode films," *APL Materials*, vol. 12, no. 6, p. 061 114, Jun. 2024, ISSN: 2166-532X. DOI: 10.1063/5.0213461. eprint: https://pubs.aip.org/aip/apm/article-pdf/doi/10.1063/5.0213461/20010468/061114_1_5.0213461.pdf. [Online]. Available: https://doi.org/10.1063/5.0213461.

[8] V. Pavlenko, J. Smedley, A. Scheinker, *et al.*, "Stoichiometry control and automated growth of alkali antimonide photocathode films by molecular beam deposition," *Applied Physics Letters*, vol. 120, no. 9, p. 091 901, Mar. 2022, ISSN: 0003-6951. DOI: 10.1063/5.0080948. eprint: https://pubs.aip.org/aip/apl/article-pdf/doi/10.

1063/5.0080948/16476606/091901_1_online.pdf. [Online]. Available: https://doi.org/10.1063/5.0080948.

[9] K. H. Jack and M. M. Wachtel, "The characterization and crystal structure of caesium antimonide, a photo-electric surface material," *Proceedings of the Royal Society of London. Series A, Mathematical and Physical Sciences*, vol. 239, no. 1216, pp. 46–60, 1957, ISSN: 00804630. [Online]. Available: http://www.jstor.org/stable/100179 (visited on 09/03/2024).

[10] C. W. Bates, D. Das Gupta, L. Galan, and D. Buchanan, "X-ray photoemission studies of cesium antimonide photoemitters," *Thin Solid Films*, vol. 69, no. 2, pp. 175–182, 1980, ISSN: 0040-6090. DOI: https://doi.org/10.1016/0040-6090(80)90034-6. [Online]. Available: https://www.sciencedirect.com/science/article/pii/0040609080900346.

[11] R. Tromp, J. Hannon, A. Ellis, W. Wan, A. Berghaus, and O. Schaff, "A new aberration-corrected, energy-filtered leem/peem instrument. i. principles and design," *Ultramicroscopy*, vol. 110, no. 7, pp. 852–861, 2010, ISSN: 0304-3991. DOI: https://doi.org/10.1016/j.ultramic.2010.03.005. [Online]. Available: https://www.sciencedirect.com/science/article/pii/S0304399110000835.

[12] R. Tromp, J. Hannon, W. Wan, A. Berghaus, and O. Schaff, "A new aberration-corrected, energy-filtered leem/peem instrument ii. operation and results," *Ultramicroscopy*, vol. 127, pp. 25–39, 2013, Frontiers of Electron Microscopy in Materials Science, ISSN: 0304-3991. DOI: https://doi.org/10.1016/j.ultramic.2012.07.016. [Online]. Available: https://www.sciencedirect.com/science/article/pii/S0304399112001866.

[13] J. Jobst, L. M. Boers, C. Yin, J. Aarts, R. M. Tromp, and S. J. van der Molen, "Quantifying work function differences using low-energy electron microscopy: The case of mixed-terminated strontium titanate," *Ultramicroscopy*, vol. 200, pp. 43–49, 2019, ISSN: 0304-3991. DOI: https://doi.org/10.1016/j.ultramic.2019.02.018. [Online]. Available: https://www.sciencedirect.com/science/article/pii/S0304399118304182.

[14] S. Karkare *et al.*, "Physical and Chemical Roughness of Alkali-Animonide Cathodes," *CERN*, International Particle Accelerator Conference, no. 9, pp. 4259–4262, Jun. 2018, https://doi.org/10.18429/JACoW-IPAC2018-THPMF080. DOI: doi:10.18429/JACoW-IPAC2018-THPMF080. [Online]. Available: http://jacow.org/ipac2018/papers/thpmf080.pdf.

[15] M. Sauty, C. W. Johnson, T. Tak, *et al.*, "Investigation of the cesium activation of GaN photocathodes by low-energy electron microscopy," *Phys. Rev. Appl.*, vol. 22, p. 034005, 3 Sep. 2024. DOI: 10.1103/PhysRevApplied.22.034005. [Online]. Available: https://link.aps.org/doi/10.1103/PhysRevApplied.22.034005.

[16] E. A. Taft and H. R. Philipp, "Structure in the energy distribution of photoelectrons from K3Sb and cs3Sb," *Phys. Rev.*, vol. 115, pp. 1583–1586, 6 Sep. 1959. DOI: 10.1103/PhysRev.115.1583. [Online]. Available: https://link.aps.org/doi/10.1103/PhysRev.115.1583.

[17] M. Rog, "From bipeem to uv-onem: Theory and experiment," *Leiden University*, 2022. [Online]. Available: https://hdl.handle.net/1887/3454584.

[18] F. J. Himpsel, F. R. McFeely, A. Taleb-Ibrahimi, J. A. Yarmoff, and G. Hollinger, "Microscopic structure of the SiO2/Si interface," *Phys. Rev. B*, vol. 38, pp. 6084–6096, 9 Sep. 1988. DOI: 10.1103/PhysRevB.38.6084. [Online]. Available: https://link.aps.org/doi/10.1103/PhysRevB.38.6084.

[19] R. Honig and D. Kramer, *Vapor Pressure Data for the Solid and Liquid Elements*. RCA Laboratories, David Sarnoff Research Center, 1969. [Online]. Available: https://books.google.nl/books?id=8gZLnQEACAAJ.

[20] G. Sauerbrey, "Verwendung von schwingquarzen zur wagung dunner schichten und zur mikrowagung," *Zeitschrift fur Physik*, 1959. DOI: 10.1007/BF01337937. [Online]. Available: https://doi.org/10.1007/BF01337937.

[21] R. M. Stassart, W. Mobius, K.-A. Nave, and J. M. Edgar, "The axon-myelin unit in development and degenerative disease," *Frontiers in Neuroscience*, vol. 12, 2018, ISSN: 1662-453X. DOI: 10.3389/fnins.2018.00467. [Online]. Available: https://www.frontiersin.org/journals/neuroscience/articles/10.3389/fnins.2018.00467.